

DynEarthSol2D: An efficient unstructured finite element method to study long-term tectonic deformation

E. Choi,^{1,2} E. Tan,³ L. L. Lavier,^{1,4} and V. M. Calo⁵

Received 18 October 2012; revised 24 February 2013; accepted 5 March 2013; published 9 May 2013.

[1] Many tectonic problems require to treat the lithosphere as a compressible elastic material, which can also flow viscously or break in a brittle fashion depending on the stress level applied and the temperature conditions. We present a flexible methodology to address the resulting complex material response, which imposes severe challenges on the discretization and rheological models used. This robust, adaptive, two-dimensional, finite element method solves the momentum balance and the heat equation in Lagrangian form using unstructured meshes. An implementation of this methodology is released to the public with the publication of this paper and is named DynEarthSol2D (available at <http://bitbucket.org/tan2/dynearthsol2>). The solver uses contingent mesh adaptivity in places where shear strain is focused (localization) and a conservative mapping assisted by marker particles to preserve phase and facies boundaries during remeshing. We detail the solver and verify it in a number of benchmark problems against analytic and numerical solutions from the literature. These results allow us to verify and validate our software framework and show its improved performance by an order of magnitude compared against an earlier implementation of the Fast Lagrangian Analysis of Continua algorithm.

Citation: Choi, E., E. Tan, L. L. Lavier, and V. M. Calo (2013), DynEarthSol2D: An efficient unstructured finite element method to study long-term tectonic deformation, *J. Geophys. Res. Solid Earth*, 118, 2429–2444, doi:10.1002/jgrb.50148.

1. Introduction

1.1. Overview of Numerical Techniques for Long-Term Tectonic Modeling

[2] Numerical simulation of the long-term (>10,000 years) evolution of geological structures at the crustal to lithospheric scales are denoted long-term tectonic modeling (LTM). Challenges arise in LTM because the geological structures of interest involve localized deformation at plate boundaries such as narrow fault and shear zones (e.g., ≤ 1 km) within a domain of a much larger scale (e.g., ≥ 100 km). To mechanically describe materials exhibiting strain localization, nonlinear rheologies are commonly used, which include power-law viscosity [e.g., Montési, 2003; Behn *et al.*, 2002], damage [e.g., Lyakhovsky *et al.*, 1993, 2012], or strain-weakening plasticity based on

Mohr-Coulomb models for frictional materials [e.g., Poliakov *et al.*, 1994; Poliakov and Buck, 1998]. The materials that compose the Earth's lithosphere are brittle when temperature and confining pressure are low but exhibit ductility when any of these thermodynamic variables are high [e.g., Jaeger and Cook, 1976; Scholz, 1988]. LTM should address these severe transitions as well as variable stiffness within each of the brittle and ductile regimes. Simulation techniques for LTM must also account for large amounts of deformation whether localized or distributed.

[3] Assessing the predictive power of new rheologies is another fundamental issue in LTM since no agreement has been reached in the scientific community on the first-order structure of the Earth's continental lithosphere. For example, the geodynamics community is presently addressing whether loads are supported by a strong crust and mantle lithosphere separated by a weak fluid-like lower crust [e.g., Watts and Burov, 2003] or by a strong upper crustal layer sitting on top of weaker lower crust and mantle lithosphere [e.g., Scholz, 2002; Bourne *et al.*, 1998]. Many studies focused on lithospheric rheology have shown that the metamorphic and magmatic reactions involving hydrous fluids as well as the polymineralic nature of rocks can control the rheological behavior of the lithosphere through time and space [e.g., Handy, 1990; Lavier and Manatschal, 2006; Ranalli, 1997]. This rheological evolution is not taken into account by the monomineralic rheological flow laws usually used in geodynamic modeling [e.g., Ranalli, 1995; Kohlstedt *et al.*, 1995]. LTM simulators may be used as test beds for new rheological models for the flow of rocks,

¹Institute for Geophysics, Jackson School of Geosciences, University of Texas, Austin, Texas, USA.

²Now at Center for Earthquake Research and Information, University of Memphis, Memphis, Tennessee, USA.

³Institute of Earth Sciences, Academia Sinica, Taipei, Taiwan.

⁴Department of Geological Sciences, Jackson School of Geosciences, University of Texas, Austin, Texas, USA.

⁵King Abdullah University of Science and Technology (KAUST), Center for Numerical Porous Media, Applied Mathematics & Computational Science, and Earth Science & Engineering, Thuwal, Saudi Arabia.

Corresponding author: E. Choi, Center for Earthquake Research and Information, University of Memphis, 3890 Central Ave., Memphis, TN 38152, USA. (echoi2@memphis.edu)

©2013. American Geophysical Union. All Rights Reserved.
2169-9313/13/10.1002/jgrb.50148

as exemplified in studies of rifting [e.g., *Huismans and Beaumont*, 2002; *Lavier and Manatschal*, 2006]. In the long run, for LTM simulations to be able to answer these open questions about the structure of the continental lithosphere, preference will be given to numerical techniques that can implement these complex nonlinear rheologies with ease.

[4] The available numerical techniques for LTM can be largely divided into two groups. The first group models the material response as elastoviscoplastic (EVP), where the brittle behavior is modeled by strain-weakening elastoplasticity and/or damage, while the ductile behavior is modeled by Maxwell viscoelasticity [e.g., *Albert et al.*, 2000; *Poliakov and Buck*, 1998; *Gerya and Yuen*, 2007; *Popov and Sobolev*, 2008]. This material description naturally represents elastic compressibility, strain weakening, and confining pressure dependence. The second group uses viscoplastic (VP) models, ignoring the elastic response of the Earth's lithosphere entirely. These models treat lithospheric motion as a viscous flow where the material response is represented using a nonlinear viscosity. The lithosphere is modeled as a high viscosity region where the brittle behavior is mimicked by a yield stress varying with an internal variable [e.g., *Tackley*, 2000; *Čžková et al.*, 2002; *Billen and Hirth*, 2007; *Fullsack*, 1995; *van Hunen et al.*, 2001; *Braun et al.*, 2008; *Dabrowski et al.*, 2008]. There are also hybrid models which consider deviatoric components of elasticity on top of the viscoplastic model [hence, partial EVP (pEVP)] [e.g., *Gerya and Yuen*, 2007; *Moresi et al.*, 2003; *OzBench et al.*, 2008; *Kaus*, 2010].

[5] Whether the motion is described in a Lagrangian or an Eulerian framework can be another classification criterion for existing techniques for LTM although this distinction is not always clear. It is important to track free surfaces or phase boundaries in the physical domain, for instance, to study surface processes or interactions between the lithosphere and the mantle [e.g., *Kaus et al.*, 2010; *Duretz et al.*, 2011]. These tasks are an inherent part of the Lagrangian framework in the sense that no extra operations are needed. However, the large deformation involved in LTM requires remeshing in the Lagrangian framework because the numerical approximation degrades as the mesh distortion becomes severe. Similar limitations are faced by Arbitrary Eulerian-Lagrangian methods [e.g., *Fullsack*, 1995; *Moresi et al.*, 2003; *Braun et al.*, 2008; *Popov and Sobolev*, 2008]. This remeshing process needs to be handled with care. Remeshing violates the fundamental premise of the Lagrangian description of motion; that is, the material points are attached to the deforming mesh. Practically, remeshing causes numerical diffusion of the advected variables as in a naively implemented advection in the Eulerian framework. The numerical diffusion, however, can be efficiently remedied by introducing particles and letting them carry phase information as well as history-dependent variables [*Sobolev and Babeyko*, 2005; *Yamamoto et al.*, 2011; *Tan et al.*, 2012; *Popov and Sobolev*, 2008; *Fullsack*, 1995; *Moresi et al.*, 2003; *Gerya and Yuen*, 2007; *Braun et al.*, 2008; *Kaus*, 2010]. The role that particles play and the computational complexity vary among different algorithms. Although without need for remeshing, the Eulerian framework usually needs extra operations involving particles or level sets to define and keep sharp internal and external boundaries [e.g., *Gerya and Yuen*, 2007; *Braun et al.*,

2008]. There is also a wealth of literature describing Eulerian formulations of elastoplasticity [*Duddu et al.*, 2009, 2012; *Plohr and Sharp*, 1988, 1992; *Demarco and Dvorkin*, 2005; *Trangenstein and Colella*, 1991; *Trangenstein*, 1994; *Miller and Colella*, 2001, 2002]. These methodologies avoid remeshing but need to solve a larger system of equations at each time step when compared with standard Lagrangian formulations and still need special interface tracking algorithms.

[6] An inspection of the available techniques used in LTM reveals a mixed use of explicit and implicit constitutive updates. The implementation of new rheologies is relatively straightforward when an explicit constitutive update is used because it does not involve subiteration within a time step even for nonlinear constitutive models. As a result, a numerical technique that adopts explicit updates can simulate both linear and nonlinear rheologies with equal ease. This is particularly true in the case of strain-weakening elastic-plastic models, where the constitutive update is more complicated than in the effective viscosity approach often used in VP or pEVP models. This is a desirable feature of a numerical technique for LTM which, as explained earlier, should work as a test bed for new rheologies. This validation process can be applied to newly proposed models on benchmark problems as well as to established models when new data becomes available. A drawback of an explicit constitutive update is that the time step size is restricted by stability requirements. In contrast, implicit constitutive updates may involve numerically expensive iterations, and the implementation of a novel nonlinear rheology can be a challenge by itself because finding a tangent stiffness operator is not always straightforward. Nevertheless, the resulting time-stepping techniques control the time step size by accuracy requirements, not stability; thus, significantly larger time steps can be taken in the models adopting implicit constitutive updates.

1.2. Need for Compressible Elasticity in Long-Term Tectonic Modeling

[7] A fundamental difference between the available implementations of the EVP approach and the others lies in how to account for elastic (reversible) deformation. The VP approach, for instance, ignores elasticity by assuming that elastic stresses can be relaxed by flow mechanisms such as creep over a Maxwell timescale (e.g., ~ 1 My for shear modulus of 30 GPa and viscosity of 10^{24} Pa·s). Nevertheless, there is a broad range of situations in which elastic stresses are important in the overall force balance. Well-known examples include the bending of oceanic lithosphere when subducted or loaded by an island chain. These model problems can be described in the framework of the thin-plate (slender-body) approximations. In particular, the bending of an oceanic lithosphere is accurately represented by the bending of an infinite or semiinfinite thin elastic plate [e.g., *Watts*, 2001; *Turcotte and Schubert*, 2002].

[8] Aware of the need to account for elastic stresses, some researchers came up with the pEVP models where only the deviatoric component of elastic stresses are brought into the incompressible VP model [e.g., *Moresi et al.*, 2003; *OzBench et al.*, 2008; *Kaus*, 2010]. Nevertheless, the imposition of the incompressibility constraint is still too

restrictive for arbitrary motions, leading to simulation responses that are overly stiff for some loading patterns.

[9] Additionally, the volumetric component of deformation, elastic or inelastic, is important in many practical instances as evidenced, for example, by the measured Poisson's ratio (ν) of common rocks in the vicinity of 0.3 rather than 0.5 [e.g., King and Christensen, 1996]; nonisochoric phase transformations like that of peridotite to serpentine in the hydrated mantle [e.g., Hyndman and Peacock, 2003; Hetényi et al., 2011]; permanent volume change during brittle deformation of rocks [e.g., Brace et al., 1966], and thermal expansion and contraction of rocks [e.g., Korenaga, 2007; Choi et al., 2008; Schrank et al., 2012].

[10] To demonstrate the need for nonisochoric deformation in LTM, we analyze the flexure of a finite-length elastic plate as an example. Through a back-of-the-envelope calculation, we can show that an elastically incompressible plate would be overly stiff compared to a reasonably compressible counterpart. In the thin-plate theory, the maximum displacement (w_{\max}) of a fixed-length plate by force loading is inversely proportional to the flexural rigidity (D) [Turcotte and Schubert, 2002]:

$$w_{\max} \sim D^{-1}.$$

D is defined as $EH^3/12(1-\nu^2)$, where E is the Young's modulus, H is the plate's thickness, and ν is Poisson's ratio. The following holds for two plates with different Poisson's ratios if everything else is the same:

$$\frac{w_{\max,1}}{w_{\max,2}} \sim \frac{1-\nu_1}{1-\nu_2}$$

According to this relationship, elastic flexure can be underestimated in the incompressible ($\nu = 0.5$) case to be only about 67% of the flexure for $\nu = 0.25$, a more relevant value for rock modeling.

[11] In the case of an infinitely long thin plate, the difference in flexure due to different Poisson's ratios would be less noticeable because the flexure scales with $D^{-\frac{1}{4}}$ [Turcotte and Schubert, 2002]. However, the assumption of infinitely long plate does not always hold. Compounded with the rheological complexity such as layered structures and poorly understood polymimetic rheologies, continental plates have finite width and length delimited by major boundary faults. Thus, assuming the lithosphere to be elastically incompressible in LTM bears a potential error other than those associated with numerical approximation.

[12] The previous considerations in addition to the fact that the Lagrangian framework can handle free boundaries naturally and an explicit constitutive update allows for an easy implementation of complex rheologies provide critical motivations for the development of a new solver for LTM based on the explicit Lagrangian EVP approach that allows for unstructured meshing, which is the fundamental contribution reported in this work.

1.3. Need for a New Explicit Lagrangian Elastoviscoplastic Solver

[13] The combination of an explicit constitutive update, the Lagrangian reference frame, and the EVP material model has been implemented in a family of codes following the Fast Lagrangian Analysis of Continua (FLAC) algorithm [Cundall and Board, 1988]. Termed geoFLAC,

hereafter, these specific implementations of the generic FLAC algorithm [e.g., Poliakov et al., 1993] require a structured quadrilateral mesh which severely limits the meshing flexibility needed for adequately capturing strain localization with a locally refined mesh. Additionally, each quadrilateral is decomposed into two sets of overlapping linear triangles that guarantee a symmetrical response to loading but leads to redundant computations. GeoFLAC uses an explicit scheme for the time integration of the momentum equation in the dynamic form as well as for the constitutive update. All of these features bring both advantages and disadvantages and thus deserve critical assessment when inherited. For instance, the explicit time integration and stress update require small time step sizes to ensure stability, increasing the computational cost of the solution. On the other hand, the explicit schemes allow for the simple implementation of arbitrarily complex nonlinear rheologies. In spite of this ambivalence, we put more weight on the relative ease with implementing rheologies, which are almost always nonlinear in LTM. As another example, we believe that the structured quadrilateral mesh of geoFLAC can be replaced with other types of mesh for improved flexibility and performance.

[14] Through such critical evaluations of the FLAC algorithm and its implementation, we distilled a new code, DynEarthSol2D, as an extension and simplification of the geoFLAC algorithm for the EVP material model. An implementation of this methodology is released to the public with the publication of this paper and is named DynEarthSol2D (available for download at <http://bitbucket.org/tan2/dynearthsol2d>). The most notable improvement is the removal of the restrictions on meshing. As a result, we can solve problems on unstructured triangular meshes while keeping the simple explicit material update that made geoFLAC dominant in the field. The use of the state-of-the-art mesh generation tools for triangulations allows for the following: (i) adaptive mesh refinement in regions of highly localized deformation, (ii) high quality of the mesh is maintained by adjusting nodal connectivity, (iii) simple mesh refinement and unrefinement to keep the size of the computational problem in a narrow band, without seriously compromising the quality of the simulation results, and (iv) easier and more faithful tracking of curvilinear boundary, such as the Moho.

[15] The rest of the paper is structured as follows. We first describe the key components of the proposed algorithm in detail, including the newly adopted techniques like the conservative mapping via a local supermesh construction. Results from relevant benchmark tests are presented next to verify our implementation as well as to demonstrate the algorithm's versatility and excellent performance. Finally, conclusions and future work are discussed.

2. Methods

2.1. Equation of Motion

[16] The equation of motion (linear momentum balance) solved by DynEarthSol2D takes the following full dynamic form:

$$\rho \ddot{\mathbf{u}} = \nabla \cdot \boldsymbol{\sigma} + \rho \mathbf{g} \quad (1)$$

where ρ is the material density, \mathbf{u} is the velocity vector, $\boldsymbol{\sigma}$ is the total (Cauchy) stress tensor, and \mathbf{g} is the

acceleration of gravity. The dot above \mathbf{u} indicates total time derivative, while boldface indicates a vector or tensor. The spatial gradient is denoted by ∇ , the inner product between vectors is denoted by \cdot , while $\nabla \cdot$ represents the divergence operator. This equation must be complemented with appropriate boundary conditions. (In this section, we assume that the boundary conditions define a well-posed problem. In section 3, the boundary conditions are detailed for each benchmark problem.) The motion is described using a Lagrangian formulation.

[17] The momentum equation is discretized using a two-dimensional (2-D), unstructured grid based on triangles. The displacement \mathbf{x} , velocity \mathbf{u} , acceleration \mathbf{a} , force \mathbf{f} , and temperature T are defined on linear (P1) elements, while other physical quantities (e.g., stress σ and strain ϵ) and material properties (e.g., density ρ and viscosity η) are piecewise constant over the elements. Equation (1) is multiplied by a weighting function, and the product is integrated over the domain. After integrating by parts and applying Gauss theorem, we obtain the following equation for the acceleration \mathbf{a}_a of every node a :

$$m_a \mathbf{a}_a = \mathbf{f}_a = \mathbf{f}_a^{\text{int}} + \mathbf{f}_a^{\text{bc}} + \mathbf{f}_a^{\text{ext}}, \quad (2)$$

where m_a is the nodal mass given by

$$m_a = \sum_e \left(\int_{\Omega_e} N_a^e \rho_f d\Omega \right) = \sum_e \left(\rho_f \int_{\Omega_e} N_a^e d\Omega \right) = \sum_e \left(\frac{1}{M} \rho_f \Omega_e \right), \quad (3)$$

Ω_e is the area (volume in 3-D) of the element e , N_a^e is the linear shape function associated with the node a in the element e , and M is the number of apexes of an element ($M = 3$ for 2-D triangles and $M = 4$ for 3-D tetrahedra). The summation should be understood as done for all the elements having node a as an apex. A fictitious density, ρ_f , instead of the true density, ρ , is used in the definition of m_a in (3). Additionally, row sum mass lumping is applied to obtain a diagonal mass matrix in (3). We discuss the definition of ρ_f in section 2.1.2. The total force \mathbf{f}_a is composed of three parts: the internal, boundary, and external forces. The internal force, $\mathbf{f}_a^{\text{int}}$, is defined as follows:

$$\begin{aligned} \mathbf{f}_a^{\text{int}} &= \sum_e \left(\int_{\Omega_e} \frac{\partial N_a^e}{\partial \mathbf{x}} \cdot \boldsymbol{\sigma} d\Omega \right) = \sum_e \left(\frac{\partial N_a^e}{\partial \mathbf{x}} \cdot \boldsymbol{\sigma} \int_{\Omega_e} d\Omega \right) \\ &= \sum_e \left(\frac{\partial N_a^e}{\partial \mathbf{x}} \cdot \boldsymbol{\sigma} \Omega_e \right). \end{aligned} \quad (4)$$

Neumann boundary conditions are tractions prescribed on the surface of the body. These tractions yield a boundary force denoted \mathbf{f}_a^{bc} :

$$\mathbf{f}_a^{\text{bc}} = \sum_e \left(\oint_{\partial \Omega_e} -N_a^e \boldsymbol{\sigma} \cdot \mathbf{n} dL \right) = - \sum_e^{a \in s, s \in \partial \Omega_e} \left(\frac{1}{M-1} \boldsymbol{\sigma}_s \cdot \mathbf{n}_s L_s \right). \quad (5)$$

The summation is over the boundary segment s , which has a length L_s (surface area in 3-D), the outward, unit normal vector \mathbf{n} , and a prescribed (constant) stress $\boldsymbol{\sigma}_s$ on the Neumann boundary. The external force, $\mathbf{f}_a^{\text{ext}}$, is given by the following:

$$\mathbf{f}_a^{\text{ext}} = \sum_e \left(\int_{\Omega_e} N_a^e \rho g d\Omega \right) = \sum_e \left(\rho g \int_{\Omega_e} N_a^e d\Omega \right) = \sum_e^{a \in e} \left(\frac{1}{M} \rho g \Omega_e \right). \quad (6)$$

[18] When deriving the equations above, we utilize the fact that ρ_f , ρ , $\frac{\partial N_a^e}{\partial \mathbf{x}}$, $\boldsymbol{\sigma}$, and \mathbf{g} are constants on each element, and these identities the following:

$$\int_{\Omega_e} d\Omega = \Omega_e, \quad \int_{\Omega_e} N_a^e d\Omega = \frac{1}{M} \Omega_e, \quad \oint_{\partial \Omega_e} N_a^e dL = \frac{1}{M-1} L_s. \quad (7)$$

We are interested in tectonic deformation, which can be properly simulated in a quasi-static fashion. Thus, we apply a technique called “dynamic relaxation,” which enables us to achieve a static equilibrium from the dynamic momentum equation by damping out the inertial force. Additionally, using “mass scaling,” we substitute the true density by a fictitious scaled density that allows us to increase the size of admissible stable time steps in the explicit time integration scheme. That is, using the resulting “scaled” acceleration and velocity, we compute an instantaneous velocity and position of each node in the mesh, which updates the model geometry at each time step. Each of these modifications is detailed in the following sections.

2.1.1. Dynamic Relaxation

[19] Given that our focus lies in LTM, high-frequency vibrations are not relevant to the overall deformation pattern. A strong and efficient damping is necessary to achieve quasi-static solutions of the dynamic equation. Complementarily, force amplification might be needed to accelerate the transient process to achieve equilibrium. Therefore, we either damp or amplify the total net force in the discretized nodal momentum equation (2) according to the direction of velocity [Cundall, 1989]:

$$m \mathbf{a}_i = (\mathbf{f}_{\text{damped}})_i = f_i - 0.8 \operatorname{sgn}(u_i) |f_i|, \quad (8)$$

where subscript i denotes the i th component of a vector and sgn denotes the signum function. The motivation for the choice of damping/amplification is based on the simple observation that in an underdamped oscillator, the direction of force is always opposite to the velocity direction, while in an overdamped system, the direction of the force is parallel to the velocity direction. We found that this choice of damping/amplification accomplishes the design goals satisfactorily (i.e., robustly and economically).

2.1.2. Mass Scaling

[20] The Courant-Friedrichs-Lowy condition imposes a fundamental limit on the time step size for an explicit time-marching scheme. In the explicit EVP approach used in DynEarthSol2D, the p -wave velocity sets the largest possible time step size. For instance, using relevant parameters for lithospheric modeling, a p -wave speed of $\sim 10^3$ m/s and an element size of $\sim 10^3$ m yield a stable time step size of ~ 1 s. With this stringent upper limit for the time step size, a typical LTM simulation would take an excessively large number of time steps to reach the targeted amount of deformation (e.g., $O(10^{13})$ steps for 1 Myrs of model time).

[21] To overcome this drawback, a mass scaling technique is applied. We adjust each nodal mass (density) to achieve a stable time step size which is orders of magnitude larger than the one allowed by the physical density, while the fictitious increase in mass keeps the inertial forces small compared with the other forces at play in these simulations. The time step size increases when the elastic wave speed, u_{elastic} , is made comparable to the tectonic speed, u_{tectonic} ,

($\sim 10^{-9}$ m/s). We achieve this time step size increase by scaling the density as follows:

$$u_{\text{elastic}} = \sqrt{K_s/\rho_f} = c_1 u_{\text{tectonic}}, \quad (9)$$

where K_s is the bulk modulus of the material, ρ_f is a fictitious scaled density, and c_1 is a constant. When c_1 is too small, that is, the density is scaled up too high, dynamic instabilities might occur. In this case, the fictitious elastic wave is too slow to relax the stress back to quasi-equilibrium; therefore, the kinetic energy becomes too large, breaking the assumption of the quasi-static state [e.g., Chung *et al.*, 1998]. When the density scaling is insufficient (i.e., c_1 is too large), the simulation becomes too time consuming. As c_1 approaches 10^{12} , the fictitious density approaches the material (true) density. The optimal value of c_1 depends on the rheology parameters, resolution, and domain size. We find that c_1 in the range of 10^4 to 10^8 is adequate for our simulation targets. Unfortunately, the choice of c_1 is currently empirical. We are working to devise a consistent way of finding the optimal value of c_1 .

2.2. Nodal Mixed Discretization

[22] The linear triangular elements used in DynEarth-Sol2D are known to suffer volumetric locking when subject to incompressible deformations [e.g., Hughes, 2000]. Since incompressible plastic or viscous flow are often needed in LTM, we adopt an antivolumetric locking correction based on the nodal mixed discretization (NMD) methodology [Detournay and Dzik, 2006; De Micheli and Mocellin, 2009].

[23] The strain rate of element e , $\dot{\epsilon}_e$, is computed from the velocity:

$$\dot{\epsilon}_{e,ij}^{t+\Delta t} = \frac{1}{2} \sum_{a \in e} \left(\frac{\partial N_a^e}{\partial x_i} u_{a,j}^{t+\Delta t} + \frac{\partial N_a^e}{\partial x_j} u_{a,i}^{t+\Delta t} \right), \quad (10)$$

where i, j are the spatial indices. The strain rate tensor can be decomposed into the deviatoric and the isotropic parts:

$$\dot{\epsilon}_e = \text{dev}(\dot{\epsilon}_e) + \frac{1}{D} \text{tr}(\dot{\epsilon}_e) \mathbf{I}, \quad (11)$$

where $\text{dev}(\cdot)$ represents an operator returning the deviatoric tensor, $\text{tr}(\cdot)$ is an operator returning the trace of the tensor, D is the number of diagonal terms of the tensor (two for 2-D case and three for 3-D or plain strain cases), and \mathbf{I} is an appropriate identity tensor. (When plane strain description is used, that is, $\epsilon_{yy} = 0$ and $\dot{\epsilon}_{yy} = 0$, but σ_{yy} can be nonzero and must be included in the calculation.)

[24] The basic idea is to average volumetric strain rate over a group of neighboring elements and then replace each element's volumetric strain rate with the averaged one. The NMD method first assigns an area (volume in 3-D) average of the trace of $\dot{\epsilon}_e$ to each node a :

$$\dot{\epsilon}_a = \frac{\sum_{e \in e} \text{tr}(\dot{\epsilon}_e) \Omega_e}{\sum_e \Omega_e}. \quad (12)$$

Then, the nodal field $\dot{\epsilon}_a$ is interpolated back to the element to retrieve an averaged volumetric strain rate for an element e :

$$\bar{\dot{\epsilon}}_e = \sum_{a \in e} \frac{1}{M} \dot{\epsilon}_a. \quad (13)$$

where, as before, M is the number of apexes in an element. Finally, the averaged volumetric strain rate of an element is used to modify the original strain rate tensor. The antilocking modification replaces the isotropic part with $\bar{\dot{\epsilon}}_e$:

$$\dot{\epsilon}'_e = \text{dev}(\dot{\epsilon}_e) + \frac{1}{D} \bar{\dot{\epsilon}}_e \mathbf{I}. \quad (14)$$

[25] This modified strain rate tensor substitutes the original strain rate tensor when updating strain tensor and in defining constitutive update. For the sake of brevity, we drop the prime and use $\dot{\epsilon}$ to refer the modified strain rate tensor from now on.

[26] The strain tensor ϵ is accumulated:

$$\epsilon_e^{t+\Delta t} = \epsilon_e^t + \Delta t \dot{\epsilon}_e^{t+\Delta t} \quad (15)$$

2.3. Constitutive Update

[27] The stress tensor is updated using the strain rate and strain tensors according to an appropriate constitutive relationship. Since the stress update calculations are performed at the element level, we drop the subscript e to simplify notation. The EVP material model is approximated by a composite rheology which uses viscoelastic and elastoplastic submodels. With the bulk modulus K_s , shear modulus G , viscosity η , cohesion C , and internal friction angle ϕ , we calculate the viscoelastic stress σ_{ve} and the elastoplastic stress σ_{ep} .

[28] The viscoelastic stress increment $\Delta\sigma_{\text{ve}}$ is calculated assuming a linear Maxwell material, where a total deviatoric strain increment $\Delta\epsilon$ is composed of the elastic and the viscous components, while the deviatoric stress increment is identical for each component:

$$\text{dev}(\Delta\epsilon) = \frac{\text{dev}(\Delta\sigma_{\text{ve}})}{2G} + \frac{\text{dev}(\sigma_{\text{ve}})\Delta t}{2\eta} \quad (16)$$

Substituting $\Delta\epsilon$ with $\epsilon^{t+\Delta t} - \epsilon^t$, $\Delta\sigma_{\text{ve}}$ with $\sigma_{\text{ve}}^{t+\Delta t} - \sigma^t$, and σ_{ve} with $(\sigma_{\text{ve}}^{t+\Delta t} + \sigma^t)/2$, the equation above is reduced to the following:

$$\text{dev}(\sigma_{\text{ve}}^{t+\Delta t}) = \frac{\left(1 - \frac{G\Delta t}{2\eta}\right) \text{dev}(\sigma^t) + 2G \cdot \text{dev}(\epsilon^{t+\Delta t} - \epsilon^t)}{1 + \frac{G\Delta t}{2\eta}} \quad (17)$$

The isotropic stress components are updated based on the volume change. As a result, the viscoelastic stress is the following:

$$\sigma_{\text{ve}}^{t+\Delta t} = \text{dev}(\sigma_{\text{ve}}^{t+\Delta t}) + \Delta t K_s \text{tr}(\dot{\epsilon}^{t+\Delta t}) \mathbf{I}. \quad (18)$$

[29] The elastoplastic stress σ_{ep} is computed using linear elasticity and the Mohr-Coulomb (MC) failure criterion with a general (associative or nonassociative) flow rule. Following a standard operator-splitting scheme [e.g., Lubliner, 1990; Simo and Hughes, 2004; Wilkins, 1964], an elastic trial stress $\sigma_{\text{el}}^{t+\Delta t}$ is first calculated as

$$\sigma_{\text{el}}^{t+\Delta t} = \sigma^t + \left(K_s - \frac{2}{3} G \right) \text{tr}(\dot{\epsilon}^{t+\Delta t}) \mathbf{I} \Delta t + 2G \dot{\epsilon}^{t+\Delta t} \Delta t. \quad (19)$$

If the elastic trial stress, $\sigma_{\text{el}}^{t+\Delta t}$, is on or within a yield surface, that is, $f(\sigma_{\text{el}}^{t+\Delta t}) \geq 0$, where f is the yield function, then the stress does not need a plastic correction. So $\sigma_{\text{ep}}^{t+\Delta t}$ is set to be equal to $\sigma_{\text{el}}^{t+\Delta t}$. However, if $\sigma_{\text{el}}^{t+\Delta t}$ is outside the yield surface, then we project it onto the yield surface using a return-mapping algorithm [Simo and Hughes, 2004].

[30] In the case of a Mohr-Coulomb material, it is convenient to express the yield function for *shear failure* in terms of principal stresses:

$$f_s(\sigma_1, \sigma_3) = \sigma_1 - N_\phi \sigma_3 + 2C \sqrt{N_\phi}, \quad (20)$$

where σ_1 and σ_3 are the maximal and minimal compressive principal stresses with the sign convention that tension is positive (i.e., $\sigma_1 \leq \sigma_2 \leq \sigma_3$), C is the material's cohesion, $N_\phi = \frac{1+\sin\phi}{1-\sin\phi}$, $\sqrt{N_\phi} = \frac{\cos\phi}{1-\sin\phi}$, and ϕ is an internal friction angle ($< 90^\circ$). The yield function for *tensile* failure is defined as

$$f_t(\sigma_3) = \sigma_3 - \sigma_t, \quad (21)$$

where σ_t is the tension cut-off. If a value for the tension cut-off is given as a parameter, then the smallest value between the theoretical limit ($C/\tan\phi$) and the given value is assigned to σ_t . This comparison is required because the theoretical limit is not constant in the strain-weakening case, where the material cohesion, C , and the friction angle ϕ may change.

[31] To guarantee a unique decision on the mode of yielding (shear versus tensile), we define an additional function, $f_h(\sigma_1, \sigma_3)$, which bisects the obtuse angle made by two yield functions on the σ_1 - σ_3 plane, as

$$f_h(\sigma_1, \sigma_3) = \sigma_3 - \sigma_t + \left(\sqrt{N_\phi^2 + 1} + N_\phi \right) \left(\sigma_1 - N_\phi \sigma_t + 2C \sqrt{N_\phi} \right). \quad (22)$$

Once yielding is identified, that is, $f_s(\sigma_{\text{el},1}, \sigma_{\text{el},3}) < 0$ or $f_t(\sigma_{\text{el},3}) > 0$, the mode of failure (shear or tensile) is decided based on the value of f_h ; in other words, shear failure occurs if $f_h(\sigma_{\text{el},1}, \sigma_{\text{el},3}) < 0$, tensile failure occurs otherwise.

[32] The flow rule for frictional materials is in general nonassociative, that is, the direction of plastic flow in the principal stress space during plastic flow is not the same as the direction of the vector normal to the yield surface. As in the definitions of yield functions, the plastic flow potential for *shear* failure in the Mohr-Coulomb model can be defined as

$$g_s(\sigma_1, \sigma_3) = \sigma_1 - \frac{1 + \sin\psi}{1 - \sin\psi} \sigma_3, \quad (23)$$

where ψ is the dilation angle. Likewise, the *tensile* flow potential is given as

$$g_t(\sigma_3) = \sigma_3 - \sigma_t. \quad (24)$$

[33] In the presence of plasticity, the total strain increment $\Delta\epsilon$ is given by

$$\Delta\epsilon = \Delta\epsilon_{\text{el}} + \Delta\epsilon_{\text{pl}}, \quad (25)$$

where $\Delta\epsilon_{\text{el}}$ and $\Delta\epsilon_{\text{pl}}$ are the elastic and plastic strain increments, respectively. The plastic strain increment is normal to the flow potential surface and can be written as

$$\Delta\epsilon_{\text{pl}} = \beta \frac{\partial g}{\partial \sigma}, \quad (26)$$

where β is the plastic flow magnitude. β is computed by requiring that the updated stress state lies on the yield surface,

$$f\left(\sigma_{\text{ep}}^{t+\Delta t}\right) = f\left(\sigma^t + \Delta\sigma_{\text{ep}}\right) = 0. \quad (27)$$

[34] In the principal component representation, $\sigma_A = E_{AB} \epsilon_B$ where σ_A and ϵ_A are the principal stress and strain, respectively, and E is a corresponding elastic moduli matrix with the following components:

$$E_{AB} = \begin{cases} K_s - \frac{2}{3}G & \text{if } A \neq B, \\ K_s + \frac{4}{3}G & \text{otherwise.} \end{cases}$$

By applying the consistency condition (27) and using $\sigma_{\text{el}}^{t+\Delta t} = \sigma^t + E \cdot \Delta\epsilon$ (in the principal component representation), we obtain the following formulae for β

$$\beta = \frac{\sigma_{\text{el},1}^{t+\Delta t} - N_\phi \sigma_{\text{el},3}^{t+\Delta t} + 2C \sqrt{N_\phi}}{\sum_B \left(E_{1B} \frac{\partial g_s}{\partial \sigma_B} - N_\phi E_{3B} \frac{\partial g_t}{\partial \sigma_B} \right)} \quad (\text{for shear failure}), \quad (28)$$

and

$$\beta = \frac{\sigma_{\text{el},3}^{t+\Delta t} - \sigma_t}{\frac{\partial g_t}{\partial \sigma_3}} \quad (\text{for tensile failure}). \quad (29)$$

Likewise, $\partial g / \partial \sigma$ takes different forms according to the failure mode:

$$\begin{aligned} \frac{\partial g}{\partial \sigma_1} &= 1 \\ \frac{\partial g}{\partial \sigma_2} &= 0 \\ \frac{\partial g}{\partial \sigma_3} &= -\frac{1 + \sin\psi}{1 - \sin\psi} \end{aligned} \quad (\text{for shear failure}), \quad (30)$$

and

$$\begin{aligned} \frac{\partial g}{\partial \sigma_1} &= 0 \\ \frac{\partial g}{\partial \sigma_2} &= 0 \\ \frac{\partial g}{\partial \sigma_3} &= 1 \end{aligned} \quad (\text{for tensile failure}). \quad (31)$$

[35] Once $\Delta\epsilon_{\text{pl}}$ is computed as in (26) using (28) and (30) or (29) and (31), σ_{ep} is updated as

$$\sigma_{\text{ep}} = \sigma_{\text{el}}^{t+\Delta t} - E \cdot \Delta\epsilon_{\text{pl}}. \quad (32)$$

in the principal component representation and transformed back to the original coordinate system.

[36] After the viscoelastic stress σ_{ve} and elastoplastic stress σ_{ep} are evaluated, we compute the second invariant of the deviatoric components of each. If the viscoelastic stress has a smaller second invariant (J_2), then σ_{ve} is used as the updated stress; otherwise, σ_{ep} is used.

[37] The fundamental deformation measures in DynEarth-Sol2D are strain rates. Thus, the stress update by rate-independent constitutive models like elastoplastic stresses need to be considered as the time-integration of the rate form of the corresponding stresses. Since a stress rate is not frame-indifferent in general, an objective (or corotational) stress rate needs to be constructed and integrated instead. The Jaumann stress rate is our choice for DynEarthSol2D among the possible objective rates because of its simplicity.

[38] The Jaumann stress rate ($\check{\sigma}$) is defined as

$$\check{\sigma} = \dot{\sigma} - \omega \cdot \sigma + \sigma \cdot \omega, \quad (33)$$

where ω is the spin tensor, which is defined as,

$$\omega_{ij} = \frac{1}{2} \left(\frac{\partial u_i}{\partial x_j} - \frac{\partial u_j}{\partial x_i} \right). \quad (34)$$

Based on this definition, the new objective stress ($\check{\sigma}^{t+\Delta t}$) is,

$$\check{\sigma}^{t+\Delta t} = \sigma^{t+\Delta t} + \Delta t (\sigma^{t+\Delta t} \cdot \mathbf{w}^{t+\Delta t} - \mathbf{w}^{t+\Delta t} \cdot \sigma^{t+\Delta t}), \quad (35)$$

where $\sigma^{t+\Delta t}$ is the updated stress equal to either σ_{ve} or σ_{ep} , depending on which has a lower value of J_2 .

2.4. Velocity and Displacement Update

[39] The velocity is updated with the damped acceleration, but subject to the prescribed velocity boundary conditions, that is:

$$\mathbf{u}_a^{t+\Delta t} = \mathbf{u}_a^t + \Delta t \mathbf{a}_a^{t+\Delta t}. \quad (36)$$

The position \mathbf{x}_a of the node a is updated by the following:

$$\mathbf{x}_a^{t+\Delta t} = \mathbf{x}_a^t + \Delta t \mathbf{u}_a^{t+\Delta t}. \quad (37)$$

[40] Since the mesh is changed, the shape function derivatives N_a^e and the element volume Ω_e are updated every time step.

2.5. Modeling Thermal Evolution

[41] Thermal evolution of lithosphere is often one of the key components of the long-term tectonics and is modeled by solving the following heat equation:

$$\rho c_p \dot{T} = k \nabla^2 T, \quad (38)$$

where T is the temperature field, while c_p and k are the heat capacity and the thermal conductivity of the lithosphere material. Multiplying by a weighting function on both sides and integrating by parts over the domain, we get

$$C_a \dot{T}_a^{t+\Delta t} = - \sum_e^{a \in e, b \in e} (k D_{ab} T_b^t \Omega_e) + \sum_e^{a \in s, s \in \partial \Omega_e} \left(\frac{1}{M-1} \mathbf{q}_s \cdot \mathbf{n}_s L_s \right), \quad (39)$$

where the diffusion matrix

$$D_{ab} = \sum_{a,b \in e} \sum_i \frac{\partial N_a^e}{\partial x_i} \frac{\partial N_b^e}{\partial x_i} \quad (40)$$

is evaluated at the barycenter of each element since we use constant strain triangles (linear finite elements on simplices). The lumped thermal capacitance (mass) is given by

$$C_a = \sum_e^{a \in e} \left(\frac{1}{M} \rho c_p \Omega_e \right), \quad (41)$$

and \mathbf{q}_s is the prescribed boundary heat flux on a segment s . Then, the temperature is updated explicitly as follows:

$$T_a^{t+\Delta t} = T_a^t + \Delta t \dot{T}_a^{t+\Delta t}. \quad (42)$$

The stability condition for the explicit integration of temperature is usually satisfied by the time step size determined by the scaled wave speed, but if a stable time step size for heat diffusion is smaller, then it becomes the global time step size.

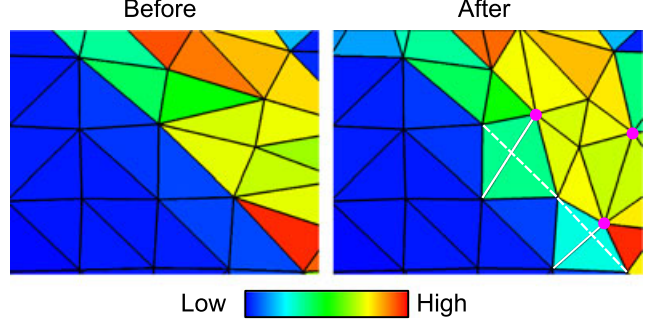


Figure 1. Images showing how edge-flipping as well as conservative mapping of a color-coded piecewise constant field is performed during remeshing. On the “After” image, white solid and dashed lines indicate example pairs of flipped and original edges, and the magenta-colored dots are nodes newly created during remeshing.

2.6. Remeshing

[42] We assess the mesh quality at fixed temporal intervals and use specific quality measures to decide whether to keep using the present mesh or remesh. For example, if the smallest angle of an element is less than a certain prescribed value, then we remesh. A group of nodes in the deformed mesh is removed from the mesh if any of the following criteria is met. For instance, if the deformed or displaced boundary is restored to the initial configuration, then some nodes may be left outside of the boundaries of the new domain. Internal nodes, if surrounded only by small elements, may be removed from the point set to be remeshed. Once all criteria are enforced, a final list of nodes is collected. These nodes are provided to the *Triangle* library [Shewchuk, 1996] to construct a new triangulation of the domain. At this stage, new nodes might be inserted into the mesh or the mesh topology changed through edge-flipping during the triangulation (Figure 1). This type of remeshing has been proposed as a way of solving large deformation problems in the Lagrangian framework [Braun and Sambridge, 1994]. After the new mesh is created, the boundary conditions, derivatives of shape function, and mass matrix have to be recalculated.

[43] When most of the deformation is focused in and around a few deformation zones like shear bands, most of the elements outside of the zones deform only slightly and thus mostly remain unaffected by remeshing. The high degree of similarity between the new and old meshes makes projecting the fields of variables between the meshes very easy. For nodes and elements unaffected by remeshing, which are the majority, a simple injection suffices. That is, the data of the nodes and elements of the old mesh are mapped onto the nodes and elements which are collocated with them in the new mesh.

[44] When deformation is not localized but distributed over a broad region of the domain, remeshing might result in a new mesh that is very different from the old one. Then, an intermesh mapping of variables becomes necessary. For data associated to nodes (e.g., velocity and temperature), we use linear interpolation of the data from the old mesh to evaluate the field at the new nodal location. For data associated to elements (e.g., strain and stress), we use a conservative

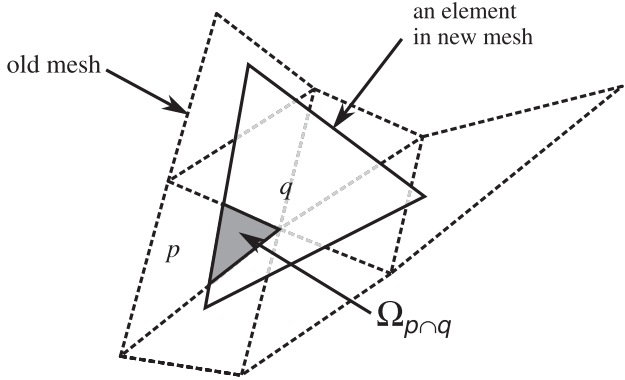


Figure 2. A new element after remeshing (q) and a set of elements in an old mesh (dotted lines) that have a nonzero intersectional area with q . As an example, an old element (p) and its intersection with q are also shown.

mapping described in the following. Given an old mesh P and a new mesh Q , the mapping is defined as follows:

$$\int_{\Omega_P} \chi d\Omega = \int_{\Omega_Q} \chi' d\Omega, \quad (43)$$

where χ is a field to be mapped to χ' , and Ω_P and Ω_Q are domains of the old and new mesh, respectively. In the finite element discretization, the above global conservative mapping boils down to the following local operation:

$$\int_{\Omega_P \cap \Omega_q} \chi d\Omega = \int_{\Omega_q} \chi' d\Omega, \quad (44)$$

where q is an element in the new mesh Q . For the linear elements used in DynEarthSol2D, variables to be mapped such as strain and stress are constant within an element. Then, the conservative mapping is further simplified to the following:

$$\chi'_q = \frac{1}{\Omega_q} \sum_{p \in P} \chi_p \Omega_{p \cap q}, \quad (45)$$

where p is an element in the old mesh P with a nonempty intersection with q , χ_p is the value of χ on the element p , and $\Omega_{p \cap q}$ is the overlapping volume of element p and q (Figure 2). The algorithms for efficiently finding the set of p and computing $\Omega_{p \cap q}$ by locally constructing a supermesh that contains both q and its intersections with p 's as subsets have been proposed [Farrell and Maddison, 2011]. We make use of these algorithms implemented in the open source library *fluidity* [Davies et al., 2011].

[45] This globally conservative remapping still induces artificial smoothing in fields that are discontinuous at a subelement level. The field of material phases is the most notable example in our case. To avoid this numerical diffusion, we generate particles to fill each element and let them carry information of such fields [Sobolev and Babeyko, 2005; Yamamoto et al., 2011; Tan et al., 2012; Popov and Sobolev, 2008; Fullsack, 1995; Moresi et al., 2003; Gerya and Yuen, 2007; Braun et al., 2008; Kaus, 2010]. The particles with phase identities set in an old mesh find a containing element in the new mesh after remeshing. A material property needed at a new element's quadrature point is computed by arithmetically or harmonically averaging the corresponding values of particles that represent each phase.

3. Discussion

3.1. Benchmarks

[46] To demonstrate the validity of our numerical method, we solve a series of problems of which exact solutions are known or approximate solutions are available, reported in the literature or acquired from an independent code, so that we can quantitatively compare these solutions with those obtained with DynEarthSol2D. The solved problems include the following:

- [47] 1. Flexure of a finite-length elastic plate;
- [48] 2. Thermal diffusion of half-space cooling plate;
- [49] 3. Stress build-up in Maxwell viscoelastic material;
- [50] 4. Rayleigh-Taylor instability;
- [51] 5. Mohr-Coulomb oedometer test; and
- [52] 6. Modes of core complex formation.

3.1.1. Flexure of a Finite-Length Elastic Plate

[53] An elastic plate is loaded in a fashion often encountered in LTM [e.g., Albert et al., 2000], where a 50 km long and 5 km thick elastic plate is pushed up from below at one end by a buoyant body (Figure 3a). The plate's shear modulus is 30 GPa, and density is 2700 kg/m³. The plate is floating over a low-viscosity (10¹⁷ Pa·s) layer. The buoyant body is a 5 × 5 km square block with a reduced density (70 % of the plate's density) but with the same elastic stiffness. The buoyant block is placed at the right-end base of the plate, generating an upward gravitational load.

[54] The total relief generated by the load converges to 306 and 370 m for the nearly incompressible ($v = 0.495$) and the compressible ($v = 0.25$) cases, respectively, when the resolution is at least 146 m (Figure 3b). Furthermore, we acquired a converged total relief of 308 m from a resolution

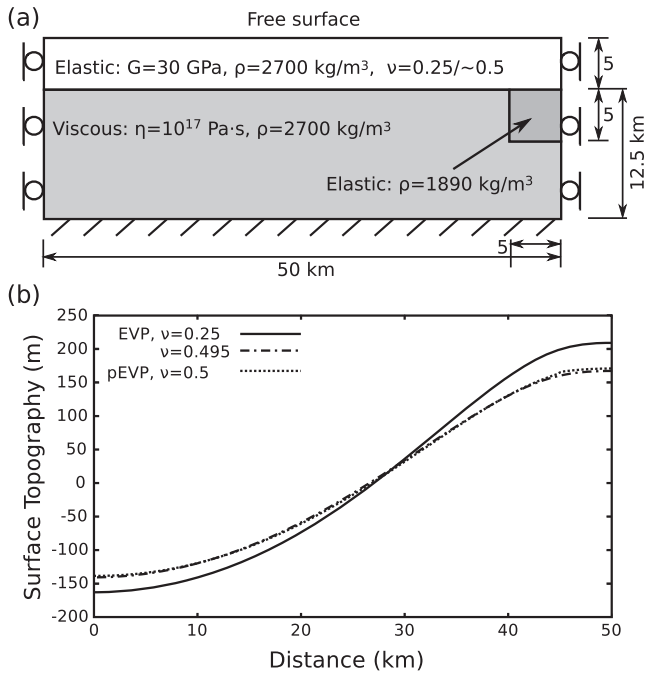


Figure 3. Effect of elastic compressibility on the prediction of an elastic thin plate subject to an uplifting load. (a) Model setup for a finite length elastic layer subjected to a finite length buoyant load applied on the bottom. (b) Profiles of mean-subtracted surface topography.

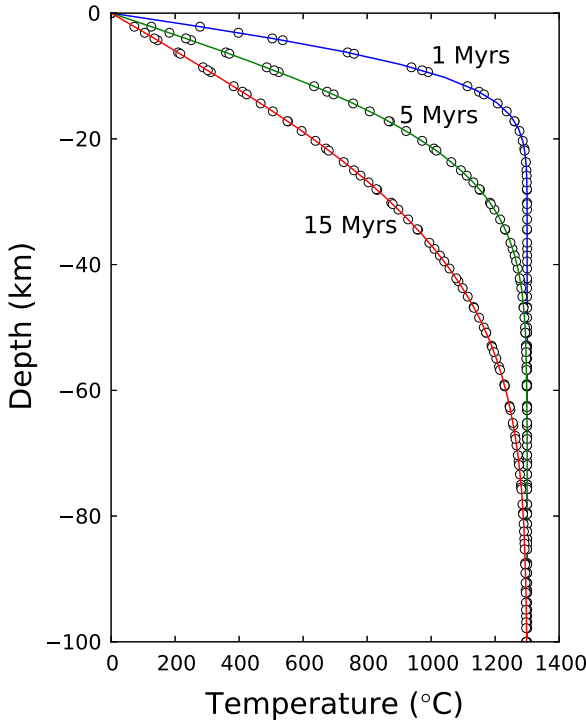


Figure 4. Thermal diffusion of half space cooling plate. The temperature profiles in the analytical solution at 1, 5, and 15 Myrs are plotted in solid lines. The results from DynEarthSol2D are plotted in circles.

of at least 140 m with the marker-in-cell pEVP approach [Petersen et al., 2010] and completely incompressible elasticity (i.e., $\nu = 0.5$) (Figure 3b). The reliefs for the (nearly) incompressible cases are consistently about 83 % of those for the compressible cases. These results indicate that the ignored compressibility in elasticity renders the plate over-stiff to bending, which is a locking phenomenon due to material description, not numerical discretization.

3.1.2. Thermal Diffusion of Half-Space Cooling Plate

[55] This simple case tests the implementation of the discrete system defined by equations (39)–(42). The initial

temperature profile is based on the half-space cooling of a 1 Myr-old plate with $\rho = 1000 \text{ kg/m}^3$, $c_p = 1000 \text{ J/kg/K}$, $k = 1 \text{ J/m/K}$, surface temperature $T_0 = 0^\circ\text{C}$, and mantle temperature $T_m = 1300^\circ\text{C}$. The analytical solution of the temperature profile [Turcotte and Schubert, 2002] is given as follows:

$$T(z) = T_0 + (T_0 - T_m) \operatorname{erf}\left(\frac{z}{2\sqrt{\frac{kt}{\rho c_p}}}\right)$$

The temperature profiles at 5 Myrs and 15 Myrs from DynEarthSol2D are compared with the analytical solution in Figure 4, and they show excellent agreement.

3.1.3. Stress Build-up in Maxwell Viscoelastic Material

[56] We demonstrate the validity of dynamic relaxation and mass scaling used in our numerical method by computing a quasi-static stress build-up process with Maxwell rheology. This test is based on the first test example in Gerya and Yuen [2007]. An incompressible, viscoelastic (Maxwell) medium is subject to pure shear at a constant strain rate. The analytical solution of the deviatoric stress is given by the following:

$$\sigma = 2\dot{\epsilon}\eta(1 - e^{-Gt/\eta}).$$

[57] The numerical result is obtained with a grid size of 251 nodes and 441 elements. The parameters used in the calculation are the following: $\dot{\epsilon} = 10^{-14} \text{ s}^{-1}$, $\eta = 10^{22} \text{ Pa} \cdot \text{s}$, $G = 10^{10} \text{ Pa}$, $K_s = 10^{12} \text{ Pa}$ (to approximate incompressibility), $\mathbf{g} = 0 \text{ m/s}^2$, and $c_1 = 10^{-6}$. The comparison (Figure 5) of the numerical result against the analytical solution establishes the validity of our numerical method and the accuracy of the Maxwell rheology implementation.

3.1.4. Rayleigh-Taylor Instability

[58] To further test the Maxwell viscoelastic rheology in the limit of purely viscous flow, we benchmark our solver by modeling a Rayleigh-Taylor instability for two fluids which have identical viscosity following the study of van Keken et al. [1997] (referred to as “VK” hereafter). The viscous convection is a Stokes problem, where the inertial term in equation (1) is negligible and force equilibrium is achieved at any instant of time. We use this problem to demonstrate the efficacy of our damping to reach static equilibrium, especially after remeshing.

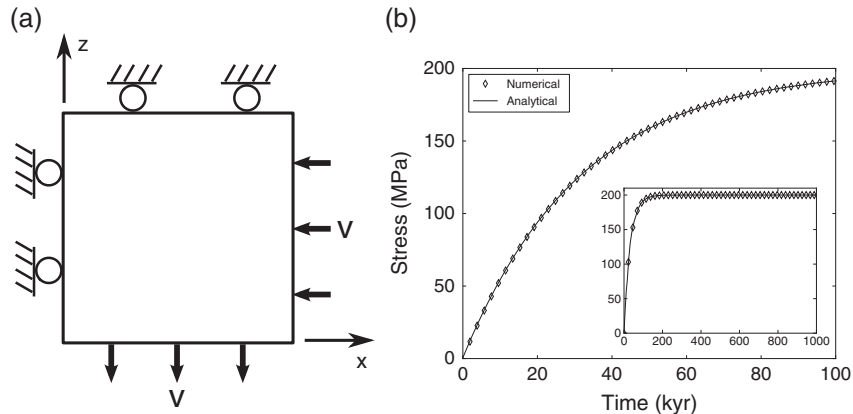


Figure 5. Stress build-up in Maxwell viscoelastic material. (a) Model setup. (b) The curve shows the evolution of stress buildup as a function of time. The numerical results in the inset are plotted less frequently.

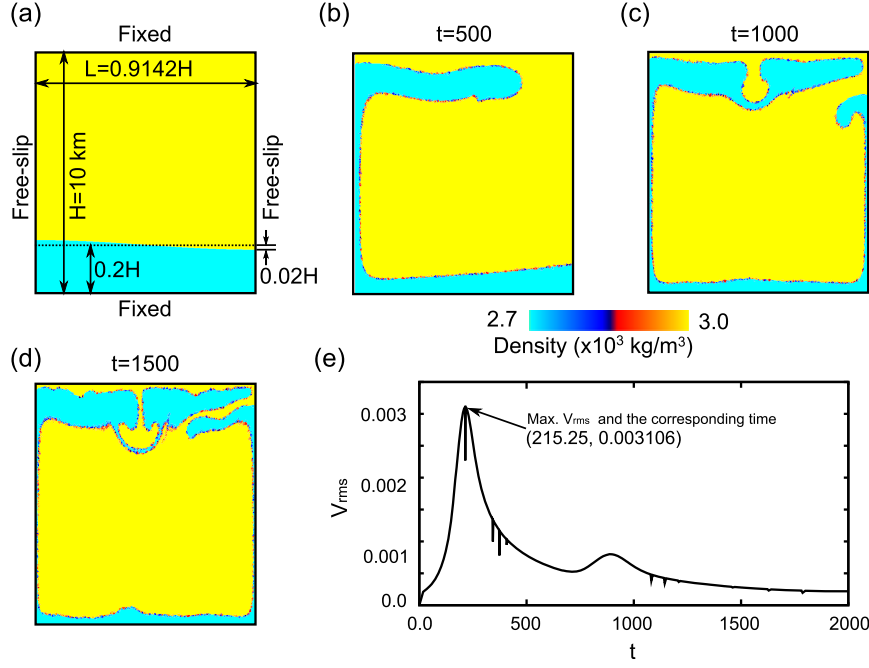


Figure 6. Rayleigh-Taylor instability. (a) Model setup. Snapshots of the density at dimensionless time of (b) 500, (c) 1000, and (d) 1500. (e) Plot of V_{rms} versus dimensionless time, t . The resolution is about 0.6 km. The results are in good agreement with benchmarks published by [van Keken *et al.*, 1997; Babeyko *et al.*, 2002].

[59] Figure 6(a) shows the model setup that includes the domain height (H) of 10 km, the aspect ratio of the domain, 0.9142, and boundary conditions. The lower layer takes up 20 % of the domain volume and is 10 % less dense than the upper layer of density 3000 kg/m^3 . The initial geometry of the interface between the layers is perturbed by a cosine function with an amplitude of 2 % of H . The viscosity is uniform throughout and equal to $10^{17} \text{ Pa} \cdot \text{s}$.

[60] Since the original benchmark test assumed a purely viscous material, we modify the elastic and viscous properties following Poliakov *et al.* [1993] to minimize the influence from the elastic component in the Maxwell model. Key nondimensional numbers are the Deborah number (De) defined as the ratio of relaxation time to advection time (see Table 1 for the precise expression) and the Reynolds number (Re) which relates viscous to inertial forces. In our simulations, to scale the fictitious density, we prescribe Re as it relates density and velocity. We set Re to be 0.01 to ensure compatibility with the original viscous flow [Poliakov *et al.*,

1993; Babeyko *et al.*, 2002]. With the parameters listed in Table 1, we get $De = 0.01$, which ensures that the material in the model behaves viscously [Poliakov *et al.*, 1993]. Time and velocity are nondimensionalized by the characteristic advection time, τ_a (see Table 1 for definition) and the characteristic velocity, H/τ_a .

[61] Snapshots from a DynEarthSol2D model with $\sim 67 \text{ m}$ resolution are shown at nondimensional times 500, 1000, and 1500 (Figures 6b–6d). They exhibit a good match with those in the original benchmark tests of VK. The root mean square velocity (V_{rms}) is defined as

$$V_{\text{rms}} = \sqrt{\frac{1}{\Omega} \int_{\Omega} \|\mathbf{u}\|^2 d\Omega},$$

where $\|\mathbf{u}\|$ is the L_2 norm of a velocity vector \mathbf{u} , and Ω is the area of the domain. The temporal variation of V_{rms} is shown in Figure 6e and is consistent with the results of VK. From DynEarthSol2D, the times that correspond to the maximum V_{rms} are 0.003106 and 215.3, respectively. A coarser resolution model ($\sim 100 \text{ m}$) gave 0.003101 and 215.28. So the relative error between solutions for these two resolutions are less than 0.1%. The “best” model in VK gave 0.003091 and 207.05. While the maximum V_{rms} values are close to each other, the corresponding time from DynEarthSol2D differs by about 4% relative to the best model. However, this difference is still within the range shown by various models tested in VK. The sudden dips of V_{rms} occur right after remeshing, when the interpolated stress on the new mesh is not in equilibrium. However, our efficient damping quickly restores the force balance without overshoots.

[62] The remeshing scheme described in section 2.6 along with the use of markers to carry compositional

Table 1. Model Parameters for the Rayleigh-Taylor Instability

Parameter	Symbol	Value
Reference density	ρ_0	3000 kg/m^3
Density difference	$\Delta\rho$	300 kg/m^3
Gravitational acceleration	g	10 m/s^2
Bulk modulus	K	50 GPa
Shear modulus	G	50 GPa
Viscosity	η	$10^{17} \text{ Pa} \cdot \text{s}$
Length scale	H	10 km
Relaxation time scale	τ_r	$\eta/G = 3 \times 10^8 \text{ s}$
Advection time scale	τ_a	$\eta/(\Delta\rho g H) = 3 \times 10^{10} \text{ s}$
Deborah number	De	$\tau_r/\tau_a = 0.01$
Reynolds number	Re	$\rho_f H^2 / (\tau_a \eta) = 0.01$

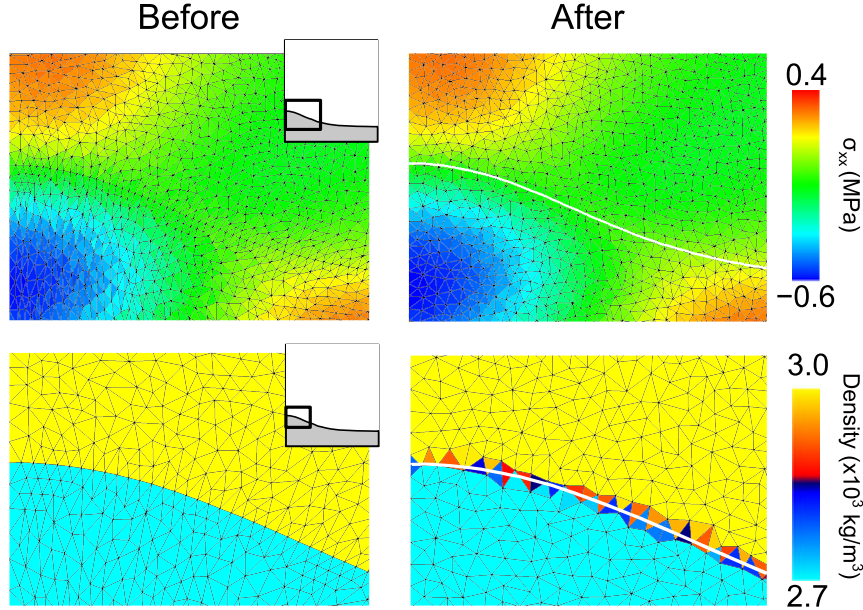


Figure 7. σ_{xx} and density fields before and after the first remeshing in the Rayleigh-Taylor instability model with about 1 km resolution. The white lines in the “After” images denote the original phase boundary before remeshing. The thick-lined box in the inset shows the location of the zoomed-in part of the domain.

variables allows us to model extremely large mesh deformation without artificial diffusion, as exemplified in Figure 7. In this figure, the horizontal (σ_{xx}) stress (top) and the density (bottom) fields are transferred from a mesh which tracked the material interface (labeled “Before”), to one which does not capture the interface explicitly (labeled “After”). As shown in Figure 7, the new mesh has excellent quality, while the material interface blurring is limited to the elements cut by the interface.

3.1.5. Plastic Oedometer Test

[63] In an oedometer test, a square block (1×1 m) of Mohr-Coulomb (MC) plastic material is compressed (Figure 8a). The compression is driven by a constant velocity, 10^{-5} m/s, applied on one side, while the other sides can slip freely. Due to symmetry, σ_1 , the most compressive principal stress, coincides with σ_{xx} , while the other two principal stresses, σ_2 and σ_3 , are equal. As a result, starting from the initial unstressed state, the stress developing in the block follows a trajectory like the one shown in Figure 8b. Under these assumptions, the numerical solutions obtained using DynEarthSol2D can be compared with the analytic solution for the stresses (Appendix A). The post-yielding portion of the stress trajectory corresponds to one of the edges of the angular MC yield envelope. Since the surface normal is not uniquely determined there, this situation poses a challenge for numerical simulations of the Mohr-Coulomb plasticity. Thus, this test is also useful for verifying that DynEarthSol2D is not affected by the nonsmooth geometry of the Mohr-Coulomb yield surface. The rest of the model parameters we use are listed in Table 2.

[64] In Figure 8c, σ_{xx} is plotted as a function of the displacement in x . The DynEarthSol2D simulation results are in excellent agreement with the analytic solution. Brittle deformations of rocks often accompany permanent volume change which is modeled using a nonzero dilation

angle. DynEarthSol2D can accurately and robustly model the behavior of a Mohr-Coulomb material for arbitrary dilation angles.

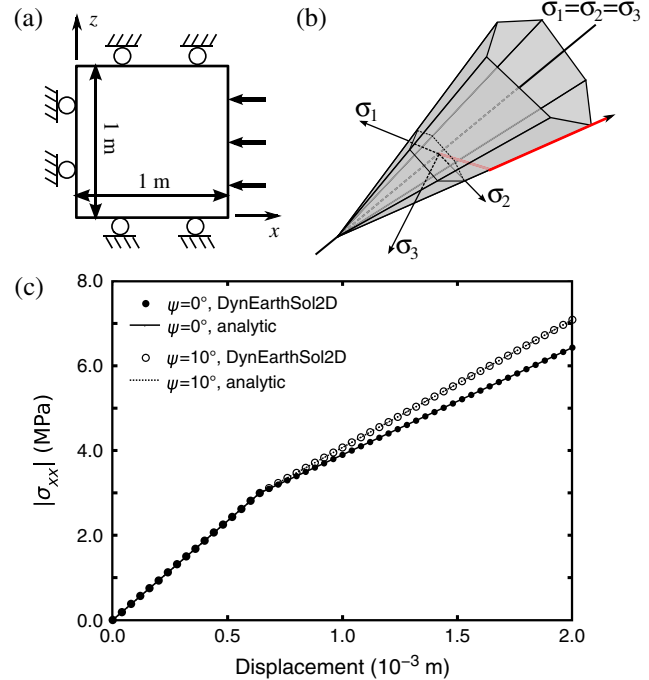


Figure 8. Plastic oedometer test. (a) Model setup. (b) A schematic trajectory of stress (red line) expected from the oedometer test in the principal stress space. A Mohr-Coulomb failure envelope is also shown. (c) $|\sigma_{xx}|$ versus x -displacement curves from analytic and numerical solutions by DynEarthSol2D.

Table 2. Model Parameters for the Oedometer Test

Parameter	Symbol	Value
Bulk modulus	K	200 MPa
Shear modulus	G	200 MPa
Cohesion	C	1 MPa
Friction angle	ϕ	10°
Dilation angle	ψ	0 or 10°

3.1.6. Normal Fault Evolution

[65] To test the applicability of DynEarthSol2D to LTM, we simulate the evolution of normal faults, which was systematically investigated by *Lavier et al.* [2000]. This exercise is particularly interesting since it tests the remeshing capability and efficiency of our solver as well as the consistency of solutions with previous studies. Localization of plastic strains induced by strain weakening is considered as a proxy to faults. Strain softening is realized by reducing the cohesion linearly from its initial value C_i to its final value C_f when the plastic shear strain is increased from zero to ϵ_c .

[66] In the first model, a fault is created in an extending Mohr-Coulomb elastic-plastic layer, which is initially 100 km long and 10 km thick (Figure 9a). Both sides of the layer are pulled at a constant velocity of 0.3 cm/yr away from the center. The bottom boundary is supported by a Winkler foundation. Given a constant compensation depth z_{comp} (usually the initial depth of the domain) and a constant hydrostatic pressure P_{comp} at z_{comp} , this bottom boundary condition gives a restoration force \mathbf{f}_a^{bc} in equation (5) to a segment s of the bottom boundary, which has a mean vertical coordinate z_s :

$$\mathbf{f}_a^{\text{bc}} = - \sum_{a \in s} \frac{1}{M-1} (P_{\text{comp}} + \rho g(z_s - z_{\text{comp}})) \hat{\mathbf{z}} \cdot \mathbf{n}_s L_s.$$

The layer is initially in lithostatic stress state, and a small weak inhomogeneity is placed at the bottom center of the layer. The values for the elastic and plastic properties are set to be the same to those in *Lavier et al.* [2000] for the case of the large offset fault (Table 3). This experiment

reproduces the formation of a core complex by a rolling hinge mechanism [Buck, 1988].

[67] A Lagrangian description of the motion makes it trivial to keep track of an evolving free surface. An accurate treatment of the resulting body forces that arise from the development of topography is critical to the evolution of a localized zone of deformation at the shear zones. To avoid unrealistically sharp reliefs, however, a diffusion-type smoothing is applied to the surface topography [Jordan and Flemings, 1991]. In this study, we use a “diffusivity” of 10^{-7} m²/s.

[68] DynEarthSol2D uses an unstructured mesh with nonuniform resolution which is refined in the proximity of the shear zone area. This refinement is achieved using a remeshing scheme described in Figures 9b–9d. The fault initially forms as a zone of high plastic strain with a dip angle of about 50° and offsets by around 2 km after 3 km of horizontal extension Figure 9b. After 10 km of extension, the exposed part of the fault rotates to a dip angle of less than 40° and accumulates about 8 km of slip (Figure 9c). Even after 21.6 km of extension, the main fault remains active and has accumulated an offset almost twice the thickness of the layer (~ 18 km).

[69] The results are consistent with those in *Lavier et al.* [2000] but acquired at a higher resolution and at much smaller computational cost. The model runs are about 10 times faster than the geoFLAC runs that resolved faults with a similar resolution. The most significant among the factors contributing to the improved performance is the nonuniform initial mesh that allows a high resolution only where faults are expected to form. Although not a rigorous comparison of performance, the results are very encouraging. This improved performance is possible due to the use of a locally refined nonuniform mesh, which is dynamically refined to preserve the mesh quality in spite of the large geometrical distortion of the physical domain (Figures 9b–9d).

[70] To resolve the mesh resolution-dependence of localization, *Lavier et al.* [2000] set cohesion to be a function of the critical fault offset (Δx_c) rather than of plastic strain. Δx_c is defined as the critical plastic strain, to which

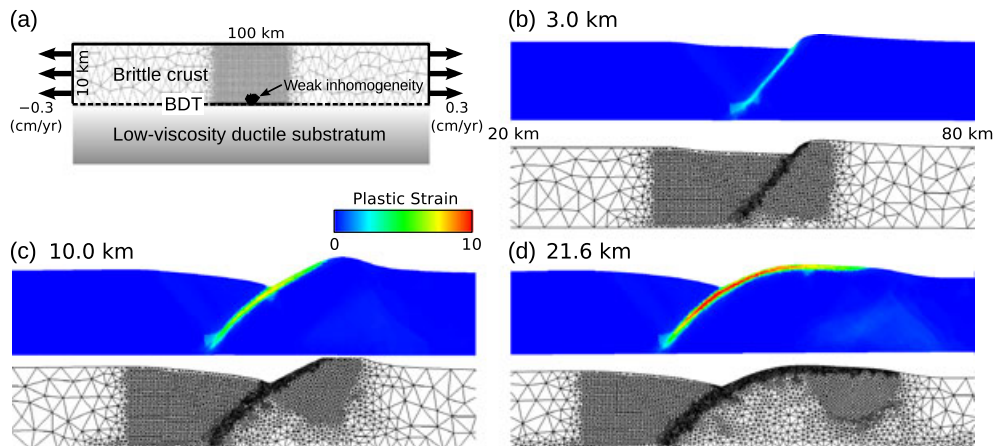


Figure 9. Normal fault evolution: Core complex formation. (a) Model setup for the large offset normal fault. Plastic strain distributions after extension of (b) 3, (c) 10, and (d) 21.6 km. Below is the evolution of the mesh as a function of the amount of extension.

Table 3. Model Parameters for the Normal Fault Evolution Tests

Parameter	Symbol	Value
Bulk modulus	K	50 GPa
Shear modulus	G	30 GPa
Density	ρ	2700 kg/m ³ (core complex/multiple fault mode)
Layer thickness	H	10/20 km
Initial cohesion	C_i	44/20 MPa
Final cohesion	C_f	4/0.1 MPa
Critical plastic strain	ϵ_c	1.2/0.5
Friction angle	ϕ	30/30°
Dilation angle	ψ	0/0°

minimum cohesion corresponds, multiplied by the width of a shear band. In a case of a uniform resolution, the width of a shear band could be identified with that of three elements on the empirical basis. However, such a static definition of the critical fault offset might not be appropriate for a mesh being dynamically refined. In this benchmark, we continued to use a static value of the critical fault offset, based on the element size of the initial mesh. As shown above, our new models produced results consistent with those from the reference study by *Lavier et al.* [2000]. Mesh refinement in this benchmark occurs only after elements in a fault zone are sheared by a large enough amount, which in turn is proportional to the accumulating fault offset. So the rate of element size reduction through remeshing must be comparable to the rate of plastic strain accumulation. This condition seems to keep the effect of dynamic mesh refinement on strain weakening at an insignificant level. Although a further investigation is needed, we speculate that results would be different for a much faster reduction in element size than a certain static rate of strain weakening.

[71] *Buck* [1993] showed that if the thickness of the layer is greater than 20 km for 20 MPa of initial cohesion, multiple faults should form during the initial evolution of the model. This contrasting behavior compared to the case of a 10 km thick layer originates from the increased bending resistance to the rolling hinge in the thick layer. We set up a second benchmark model in this category so that a layer of 200×20 km is extended as in the previous simulation. The parameters of this model are also listed in Table 3. Figure 10 shows that the extension of the thick layer results in the formation of multiple faults, which is consistent with the theoretical prediction as well as a previous numerical model (Plate 1c in *Lavier et al.* [2000]). Mesh adaptivity concentrates where the faults form and offset.

3.2. Remarks on Benchmarks

[72] We present two kinds of benchmarks that allows us to verify and validate our solver. The first kind compares numerical solutions with analytic ones for the Maxwell viscoelastic stress buildup and the Mohr-Coulomb plasticity. The second kind verifies qualitatively the consistency of solutions from our new code with the published numerical solutions in the problems of viscous chemical convection [*van Keeken et al.*, 1997] and of normal fault evolution [*Lavier et al.*, 2000]. The latter type of benchmarks is critical because there is no known analytic solution to large deformation of EVP materials in LTM. The importance of putting forward a set of relevant and reliable benchmarks cannot be overstated. Community efforts [e.g., Chapter 16 of *Gerya*,

2010, and references therein] are necessary to propose these benchmarks and to require new solver implementations to report their performance on these benchmarking tests. That is, the predictive power of elastoviscoelastic as well as of viscoplastic solvers on the agreed upon benchmarks is fundamental to allow for reproducible science. The final goal is to avoid misinterpretation of modeling behavior due to erroneous implementations of the models.

3.3. Remarks on Performance

[73] DynEarthSol2D runs only serially. A 3-D version is under development and will be parallelized via OpenMP. All the benchmarks presented above were run on one core of a Intel Core2 Quad Q9650 CPU with an operating frequency of 3.00 GHz. The largest size benchmark is the highest resolution (~ 146 m resolution) model for flexure of a finite-length elastic plate, which has 22,772 nodes and 44,897 elements. The CPU time taken for 4.32 million time steps is 176,961 s; thus, the average CPU time per time step is about 41 ms.

[74] We reported in the previous section that DynEarth-Sol2D is about 10 times faster than geoFLAC. This apparent boost in performance is due to the a priori mesh adaptation. For instance, the models for the normal fault evolution

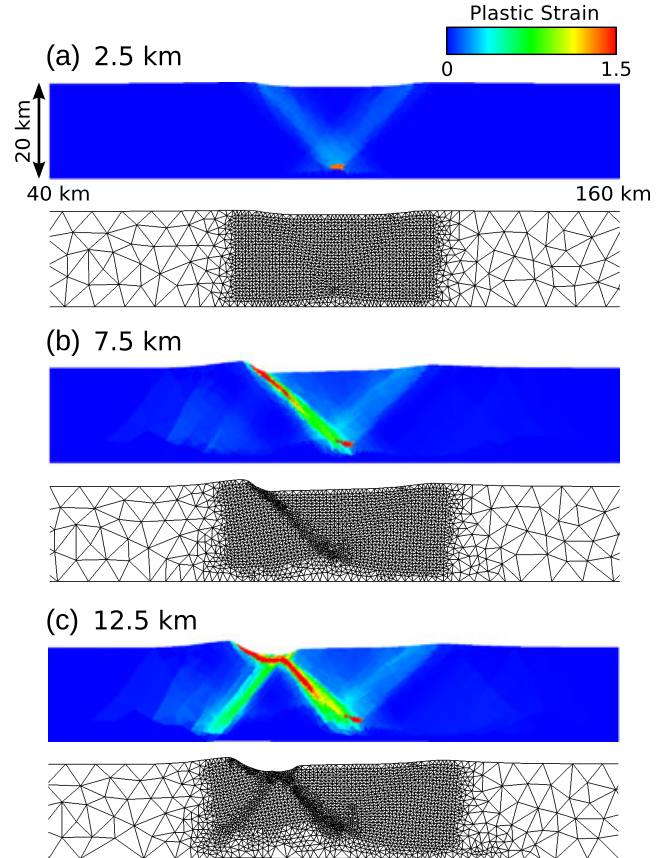


Figure 10. Normal fault evolution: Multiple faults. Plastic strain distributions after extension of (a) 2.5, (b) 7.5, and (c) 12.5 km. Below is the evolution of the mesh as a function of the amount of extension. The layer thickness is 20 km, and strain-weakening parameters are different from those of the large offset fault mode (Table 3).

started with a mesh refined around the region known to deform actively, achieving the desired resolution for faults; while the number of elements are much less than in a uniform-resolution mesh. Dynamic refinement increases the total number of elements but is also regulated by coarsening.

[75] Although we have improved the performance of existing geoFLAC-based EVP codes, it may not be the fastest possible numerical algorithm. For instance, the partial EVP marker-in-cell finite difference algorithm of Gerya [Gerya and Yuen, 2007] shows great performance especially when combined with a multigrid solver [Petersen et al., 2010]. Moreover, it is possible to implement the full EVP approach in this algorithm because it is not hardwired to solve the incompressible Stokes equation. However, this potential has yet to be realized in an actual implementation. Also, we believe that in addition to the relative ease of rheological implementation, the algorithms adopted by DynEarthSol2D deliver unique advantages such as flexibility to develop models with complex geometries since it is based on an adaptive unstructured mesh. Additionally, the use of markers allows us to reproduce complex inclusion of facies without explicitly meshing their interfaces.

4. Conclusions

[76] In this paper, we report a new Lagrangian elastoviscoelastic solver and its implementation in DynEarthSol2D for long-term tectonic deformation of the lithosphere. This new solver combines the flexibility of the explicit finite element formulation with an unstructured simplicial mesh, conservative remeshing aided by Lagrangian particles and adaptive meshing with edge-flipping. DynEarthSol2D can easily handle all the conventional rheologies of interest for lithospheric deformation including true elastic, Maxwell viscoelastic, pure viscous, and elastoplastic with associative and nonassociative plastic flow. The explicit formulation of the constitutive update makes the potential addition of other more complicated rheologies straightforward. We showed that this type of formulation more accurately renders the effects of elastic compressibility. Therefore, the amplitude of critical geologic features is better predicted, such as rift flank uplifts, bending at subduction and folding zones in mountain belts. On top of the reliability shown by benchmark results, DynEarthSol2D can be more efficient than geoFLAC through a priori and dynamic mesh refinement. Written in standard Fortan 90, this new code also allows for easy maintenance and portability. In the future, we will use a three-dimensional simplicial mesh generator to extend this algorithm to three dimensions. Our goal is to achieve the same degree of flexibility, robustness, and efficiency for complex three-dimensional simulations of lithospheric evolution.

Appendix A: Analytic Solution to the Mohr-Coulomb Oedometer Test

[77] In the setting depicted by Figure 8a, the components of the strain increments are given by

$$\begin{aligned}\Delta\epsilon_{xx} &= \frac{v_x \Delta t}{L} \\ \Delta\epsilon_{yy} = \Delta\epsilon_{zz} &= 0,\end{aligned}$$

where v_x is the x component of the velocity applied on the moving surface, L is the length of the side of the square domain, and $v_x \Delta t \ll L$ is assumed. The corresponding stress increments in the elastic regime are

$$\begin{aligned}\Delta\sigma_{xx}^{\text{el}} &= (\lambda + 2G)\Delta\epsilon_{xx} \\ \Delta\sigma_{yy}^{\text{el}} = \Delta\sigma_{zz}^{\text{el}} &= \lambda\Delta\epsilon_{xx},\end{aligned}\quad (\text{A1})$$

where the Lamé constant $\lambda = K_s + \frac{2}{3}G$ is used to simplify the equations. Moreover, stresses at any time t before yielding are given as

$$\begin{aligned}\sigma_{xx}^{\text{el}} &= (\lambda + 2G)\frac{v_x t}{L} \\ \sigma_{yy}^{\text{el}} = \Delta\sigma_{zz}^{\text{el}} &= \lambda\frac{v_x t}{L},\end{aligned}$$

while at the yielding, the stresses defined above make the following two yield functions simultaneously zero:

$$\begin{aligned}f_{s,1}(\sigma_{xx}, \sigma_{yy}) &= \sigma_{xx} - N_\phi \sigma_{yy} + 2C\sqrt{N_\phi} \\ f_{s,2}(\sigma_{xx}, \sigma_{zz}) &= \sigma_{xx} - N_\phi \sigma_{zz} + 2C\sqrt{N_\phi},\end{aligned}$$

where the parameters are the same with those in equation (20). However, due to the inherent symmetry (i.e., $\sigma_{yy} = \sigma_{zz}$), it suffices to consider only one of the two yield functions. Therefore, from $f_{s,1}(\sigma_{xx}, \sigma_{yy}) = 0$, for instance, we get the following expression for the time when yielding starts:

$$t_{\text{yield}} = \frac{CL\sqrt{N_\phi}}{((\lambda + 2G) - \lambda N_\phi)|v_x|}.$$

[78] By the same token, plastic flows need to be computed from two yield potentials,

$$\begin{aligned}g_{s,1}(\sigma_{xx}, \sigma_{yy}) &= \sigma_{xx} - N_\psi \sigma_{yy} \\ g_{s,2}(\sigma_{xx}, \sigma_{zz}) &= \sigma_{xx} - N_\psi \sigma_{zz}.\end{aligned}$$

Then, plastic strain increments are given as

$$\begin{aligned}\Delta\epsilon_{xx}^{\text{pl}} &= \beta_1 \frac{\partial g_{s,1}}{\partial \sigma_{xx}} + \beta_2 \frac{\partial g_{s,2}}{\partial \sigma_{xx}} = \beta_1 + \beta_2 = 2\beta \\ \Delta\epsilon_{yy}^{\text{pl}} &= \beta_1 \frac{\partial g_{s,1}}{\partial \sigma_{yy}} = -\beta_1 N_\psi = -\beta N_\psi \\ \Delta\epsilon_{zz}^{\text{pl}} &= \beta_2 \frac{\partial g_{s,2}}{\partial \sigma_{zz}} = -\beta_2 N_\psi = -\beta N_\psi,\end{aligned}$$

where the inherent symmetry is utilized again to identify β_1 with β_2 and denote them as β . Collecting the previous results, we conclude that the stress increments after yielding are the following:

$$\begin{aligned}\Delta\sigma_{xx} &= (\lambda + 2G)\Delta\epsilon_{xx}^{\text{el}} + \lambda (\Delta\epsilon_{yy}^{\text{el}} + \Delta\epsilon_{zz}^{\text{el}}) \\ \Delta\sigma_{yy} &= (\lambda + 2G)\Delta\epsilon_{yy}^{\text{el}} + \lambda (\Delta\epsilon_{xx}^{\text{el}} + \Delta\epsilon_{zz}^{\text{el}}) \\ \Delta\sigma_{zz} &= (\lambda + 2G)\Delta\epsilon_{zz}^{\text{el}} + \lambda (\Delta\epsilon_{xx}^{\text{el}} + \Delta\epsilon_{yy}^{\text{el}}).\end{aligned}$$

By substituting the expressions for the elastic strain increments into the above equations,

$$\begin{aligned}\Delta\epsilon_{xx}^{\text{el}} &= \Delta\epsilon_{xx} - \Delta\epsilon_{xx}^{\text{pl}} = \frac{v_x \Delta t}{L} - 2\beta \\ \Delta\epsilon_{yy}^{\text{el}} &= \Delta\epsilon_{yy} - \Delta\epsilon_{yy}^{\text{pl}} = \beta N_\psi \\ \Delta\epsilon_{zz}^{\text{el}} &= \Delta\epsilon_{zz} - \Delta\epsilon_{zz}^{\text{pl}} = \beta N_\psi,\end{aligned}$$

we get

$$\begin{aligned}\Delta\sigma_{xx} &= (\lambda + 2G) \left(\frac{v_x \Delta t}{L} - 2\beta \right) + 2\lambda\beta N_\psi \\ \Delta\sigma_{yy} = \Delta\sigma_{zz} &= (\lambda + 2G)\beta N_\psi + \lambda \left(\frac{v_x \Delta t}{L} + (N_\psi - 2)\beta \right).\end{aligned}\quad (\text{A2})$$

Now, we solve the following incremental consistency condition for β :

$$\Delta f_{s,1}(\Delta\sigma_{xx}, \Delta\sigma_{yy}) = \Delta\sigma_{xx} - N_\phi \Delta\sigma_{yy} = 0.$$

Thus, the closed form expression for β may be given as

$$\beta = \frac{(\lambda + 2G) - \lambda N_\phi}{2(\lambda + G)N_\phi N_\psi + 2(\lambda + 2G) - 2(N_\phi + N_\psi)\lambda} \frac{|v_x|}{L} \Delta t. \quad (\text{A3})$$

[79] Once β is known from (A3), pre-yielding and post-yielding stresses, (A1) and (A2), are completely determined and can be plotted as a function of displacement in x as shown in Figure 8c.

[80] **Acknowledgments.** The authors would like to acknowledge the useful discussions we had with Nathan Collier from NumPor. EC would like to thank Kenni Dinesen Pettersen for generously providing his particle-in-cell code. ET is supported by Grant 101-2116-M-001-038-MY3 from the National Science Council, Taiwan. This work was supported in part by the Academic Excellence Alliance program award to Luc L. Lavier from King Abdullah University of Science and Technology (KAUST) Global Collaborative Research under the title “3-D numerical modeling of the tectonic and thermal evolution of continental rifting.” This is UTIG contribution 2563.

References

- Albert, R. A., R. J. Phillips, A. J. Dombard, and C. D. Brown (2000), A test of the validity of yield strength envelope with an elastoviscoplastic finite element model, *Geophys. J. Int.*, **140**, 399–409.
- Babeyko, A. Y., S. V. Sobolev, R. B. Trumbull, O. Oncken, and L. L. Lavier (2002), Numerical models of crustal scale convection and partial melting beneath the Altiplano–Puna plateau, *Earth Planet. Sci. Lett.*, **199**, 373–388, doi:10.1016/S0012-821X(02)00597-6.
- Behn, M. D., J. Lin, and M. T. Zuber (2002), A continuum mechanics model for normal faulting using a strain-rate softening rheology: Implications for thermal and rheological controls on continental and oceanic rifting, *Earth Planet. Sci. Lett.*, **202**(3–4), 725–740, doi:10.1016/S0012-821X(02)00792-6.
- Billen, M. I., and G. Hirth (2007), Rheologic controls on slab dynamics, *Geochem. Geophys. Geosyst.*, **8**, Q08,012, doi:10.1029/2007GC001597.
- Bourne, S. J., P. C. England, and B. Parsons (1998), The motion of crustal blocks driven by flow of the lower lithosphere and implications for slip rates of continental strike-slip faults, *Nature*, **391**, 655–659, doi:10.1038/35556.
- Brace, W. F., B. W. Paulding, Jr., and C. H. Scholz (1966), Dilatancy in the fracture of crystalline rocks, *J. Geophys. Res.*, **71**(16), 3939–3953.
- Braun, J., and M. Sambridge (1994), Dynamical Lagrangian Remeshing (DLR): A new algorithm for solving large strain deformation problems and its application to fault-propagation folding, *Earth Planet. Sci. Lett.*, **124**(1–4), 211–220, doi:10.1016/0012-821X(94)00093-X.
- Braun, J., C. Thieulot, P. Fullsack, M. DeKool, C. Beaumont, and R. Huismans (2008), DOUAR: A new three-dimensional creeping flow numerical model for the solution of geological problems, *Phys. Earth Planet. Inter.*, **171**, 76–91, doi:10.1016/j.pepi.2008.05.003.
- Buck, W. R. (1988), Flexural rotation of normal faults, *Tectonics*, **7**(5), 959, doi:10.1029/TC007i005p00959.
- Buck, W. R. (1993), Effect of lithospheric thickness on the formation of high- and low-angle normal faults, *Geology*, **21**, 933–936.
- Choi, E., L. Lavier, and M. Gurnis (2008), Thermomechanics of mid-ocean ridge segmentation, *Phys. Earth Planet. Inter.*, **171**, 374–386, doi:10.1016/j.pepi.2008.08.010.
- Chung, W. J., J. W. Cho, and T. Belytschko (1998), On the dynamic effects of explicit FEM in sheet metal forming analysis, *Eng. Comput.*, **15**(6–7), 750–776.
- Cundall, P. A. (1989), Numerical experiments on localization in frictional materials, *Ing. Arch.*, **58**, 148–159.
- Cundall, P. A., and M. Board (1988), A microcomputer program for modeling large strain plasticity problems, in *Numerical Methods in Geomechanics*, edited by G. Swoboda, pp. 2101–2108, Balkema, Rotterdam.
- Dabrowski, M., M. Krotkiewski, and D. W. Schmid (2008), MILAMIN: MATLAB-based finite element method solver for large problems, *Geochem. Geophys. Geosyst.*, **9**, 1–24, doi:10.1029/2007GC001719.
- Davies, D. R., C. R. Wilson, and S. C. Kramer (2011), Fluidity: A fully unstructured anisotropic adaptive mesh computational modeling framework for geodynamics, *Geochem. Geophys. Geosyst.*, **12**, Q06,001, doi:10.1029/2011GC003551.
- De Micheli, P. O., and K. Mocellin (2009), A new efficient explicit formulation for linear tetrahedral elements non-sensitive to volumetric locking for infinitesimal elasticity and inelasticity, *Int. J. Numer. Methods Eng.*, **79**, 45–68, doi:10.1002/nme.2539.
- Demarco, D., and E. Dvorkin (2005), An Eulerian finite element formulation for modelling stationary finite strain elastic deformation processes, *Int. J. Numer. Methods Eng.*, **62**, 1038–1063, doi:10.1002/nme.1197.
- Detournay, C., and E. Dzik (2006), Nodal mixed discretization for tetrahedral elements, in *4th International FLAC Symposium on Numerical Modeling in Geomechanics*, edited by Hart, and Varona, vol. c, Itasca Consulting Group, Inc., Minneapolis.
- Duddu, R., L. L. Lavier, and V. M. Calo (2009), Modeling and numerical simulation of earth materials in large deformation in three dimensions, *EOS Trans. AGU*, **90**, Fall Meet. Suppl., Abstract T41C–2036.
- Duddu, R., L. L. Lavier, T. J. Hughes, and V. M. Calo (2012), A finite strain Eulerian formulation for compressible and nearly incompressible hyperelasticity using high-order B-spline finite elements, *Int. J. Numer. Methods Eng.*, **89**(6), 762–785, doi:10.1002/nme.3262.
- Duretz, T., D. A. May, T. V. Gerya, and P. J. Tackley (2011), Discretization errors and free surface stabilization in the finite difference and marker-in-cell method for applied geodynamics: A numerical study, *Geochem. Geophys. Geosyst.*, **12**, Q07,004, doi:10.1029/2011GC003567.
- Farrell, P., and J. Maddison (2011), Conservative interpolation between volume meshes by local Galerkin projection, *Comput. Methods Appl. Mech. Eng.*, **200**, 89–100, doi:10.1016/j.cma.2010.07.015.
- Fullsack, P. (1995), An arbitrary Lagrangian-Eulerian formulation for creeping flows and its application in tectonic models, *Geophys. J. Int.*, **120**, 1–23.
- Gerya, T., and D. Yuen (2007), Robust characteristics method for modelling multiphase visco-elasto-plastic thermo-mechanical problems, *Phys. Earth Planet. Inter.*, **163**, 83–105, doi:10.1016/j.pepi.2007.04.015.
- Gerya, T. V. (2010), *Introduction to Numerical Geodynamic Modelling*, 358 pp., Cambridge University Press, New York.
- Handy, M. R. (1990), The solid-state flow of polymineralic rocks, *J. Geophys. Res.*, **95**(B6), 8647–8661, doi:10.1029/JB095iB06p08647.
- Hetényi, G., V. Godard, R. Cattin, and J. A. Connolly (2011), Incorporating metamorphism in geodynamic models: The mass conservation problem, *Geophys. J. Int.*, **186**, 6–10, doi:10.1111/j.1365-246X.2011.05052.x.
- Hughes, T. J. (2000), *The Finite Element Method: Linear Static and Dynamic Finite Element Analysis*, 672 pp., Dover Publication, reprint of the Prentice-Hall, Inc., Englewood Cliffs, New Jersey, 1987 edition.
- Huismans, R., and C. Beaumont (2002), Asymmetric lithospheric extension: The role of frictional plastic strain softening inferred from numerical experiments, *Geology*, **30**(3), 211–214.
- Hyndman, R. D., and S. M. Peacock (2003), Serpentinitization of the forearc mantle, *Earth Planet. Sci. Lett.*, **212**(3–4), 417–432, doi:10.1016/S0012-821X(03)00263-2.
- Jaeger, J. C., and N. G. W. Cook (1976), *Fundamentals of Rock Mechanics*, 2nd ed., Chapman and Hall, London, United Kingdom (GBR).
- Jordan, T. E., and P. B. Flemings (1991), Large-scale stratigraphic architecture, eustatic variation, and unsteady tectonism: A theoretical evaluation, *J. Geophys. Res.*, **96**(B4), 6681–6699, doi:10.1029/90JB01399.
- Kaus, B. J. (2010), Factors that control the angle of shear bands in geodynamic numerical models of brittle deformation, *Tectonophysics*, **484**, 36–47, doi:10.1016/j.tecto.2009.08.042.
- Kaus, B. J., H. Mühlhaus, and D. A. May (2010), A stabilization algorithm for geodynamic numerical simulations with a free surface, *Phys. Earth Planet. Inter.*, **181**, 12–20, doi:10.1016/j.pepi.2010.04.007.
- King, S. D., and N. I. Christensen (1996), Physical properties of rocks, in *Encyclopedia of Earth Sciences*, edited by E. J. Dasch, MacMillan, New York.
- Kohlstedt, D. L., B. Evans, and S. J. Mackwell (1995), Strength of the lithosphere: Constraints imposed by laboratory experiments, *J. Geophys. Res.*, **100**(B9), 17,587–17,602.
- Korenaga, J. (2007), Thermal cracking and the deep hydration of oceanic lithosphere: A key to the generation of plate tectonics?, *J. Geophys. Res.*, **112**, B05,408, doi:10.1029/2006JB004502.
- Lavier, L. L., and G. Manatschal (2006), A mechanism to thin the continental lithosphere at magma-poor margins, *Nature*, **440**, 324–328, doi:10.1038/nature04608.

- Lavier, L. L., W. R. Buck, and A. N. B. Poliakov (2000), Factors controlling normal fault offset in an ideal brittle layer, *J. Geophys. Res.*, 105(B10), 23,431–23,442, doi:10.1029/2000JB900108.
- Lubliner, J. (1990), *Plasticity Theory*, 495 pp., Nacmillan, New York.
- Lyakhovsky, V., Y. Podladchikov, and P. Alexei (1993), A rheological model of a fractured solid, *Tectonophysics*, 226 (1-4), 187–198, doi:10.1016/0040-1951(93)90117-3.
- Lyakhovsky, V., A. Segev, U. Schattner, and R. Weinberger (2012), Deformation and seismicity associated with continental rift zones propagating toward continental margins, *Geochem. Geophys. Geosyst.*, 13(1), doi:10.1029/2011GC003927.
- Miller, G., and P. Colella (2001), A high-order Eulerian Godunov method for elastic-plastic flow in solids, *J. Comput. Phys.*, 167(1), 131–176, doi:10.1006/jcph.2000.6665.
- Miller, G., and P. Colella (2002), A conservative three-dimensional Eulerian method for coupled solid-fluid shock capturing, *J. Comput. Phys.*, 183(1), 26–82, doi:10.1006/jcph.2002.7158.
- Montési, L. G. J. (2003), Spacing of faults at the scale of the lithosphere and localization instability: 1. Theory, *J. Geophys. Res.*, 108(B2), 1–21, doi:10.1029/2002JB001923.
- Moresi, L. N., F. Dufour, and H.-B. Mühlhaus (2003), A Lagrangian integration point finite element method for large deformation modeling of viscoelastic geomaterials, *J. Comput. Phys.*, 184(2), 476–497, doi:10.1016/S0021-9991(02)00031-1.
- OzBench, M., et al. (2008), A model comparison study of large-scale mantle-lithosphere dynamics driven by subduction, *Phys. Earth Planet. Inter.*, 171, 224–234, doi:10.1016/j.pepi.2008.08.011.
- Petersen, K. D., S. B. Nielsen, O. R. Clausen, R. Stephenson, and T. Gerya (2010), Small-scale mantle convection produces stratigraphic sequences in sedimentary basins, *Science*, 329, 827–830, doi:10.1126/science.1190115.
- Plohr, B., and D. Sharp (1988), A conservative Eulerian formulation of the equations for elastic flow, *Adv. Appl. Math.*, 9(4), 481–499.
- Plohr, B., and D. Sharp (1992), A conservative formulation for plasticity, *Adv. Appl. Math.*, 13(4), 462–493.
- Poliakov, A., and W. R. Buck (1998), Mechanics of stretching elastic-plastic-viscous layers: Applications to slow-spreading mid-ocean ridges, in *Faulting and Magmatism at Mid-Ocean Ridges*, AGU Monograph, edited by W. R. Buck, P. T. Delaney, J. A. Karson, and Y. Lagabrielle, pp. 305–324, vol. 106, AGU, Washington D.C.
- Poliakov, A., H. Herrmann, Y. Podladchikov, and S. Roux (1994), Fractal plastic shear bands, *Fractals*, 2, 567–581.
- Poliakov, A. N. B., P. A. Cundall, Y. Y. Podladchikov, and V. A. Lyakhovsky (1993), An explicit inertial method for the simulation of viscoelastic flow: An evaluation of elastic effects on diapiric flow in two- and three-layers models, in *Flow and Creep in the Solar Systems: Observations, Modeling and Theory*, edited by D. B. Stone, and S. K. Runcorn, pp. 175–195, Kluwer Academic Publishers, Dordrecht.
- Popov, A., and S. Sobolev (2008), SLIM3D: A tool for three-dimensional thermomechanical modeling of lithospheric deformation with elasto-visco-plastic rheology, *Phys. Earth Planet. Inter.*, 171, 55–75, doi:10.1016/j.pepi.2008.03.007.
- Ranalli, G. (1995), *Rheology of the Earth*, 413 pp., Chapman & Hall, London, United Kingdom.
- Ranalli, G. (1997), Rheology of the lithosphere in space and time, *Geol. Soc. London Spec. Publ.*, 121(1), 19–37, doi:10.1144/GSL.SP.1997.121.01.02.
- Scholz, C. H. (1988), The brittle-plastic transition and the depth of seismic faulting, *Geol. Rundsch.*, 77(1), 319–328, doi:10.1007/BF01848693.
- Scholz, C. H. (2002), *The Mechanics of Earthquakes and Faulting*, 2nd ed., 496 pp., Cambridge University Press, Cambridge, U.K.
- Schrank, C. E., F. Fusseis, a. Karrech, and K. Regenauer-Lieb (2012), Thermal-elastic stresses and the criticality of the continental crust, *Geochem. Geophys. Geosyst.*, 13, 1–21, doi:10.1029/2012GC004085.
- Shewchuk, J. (1996), Triangle: Engineering a 2D quality mesh generator and Delaunay triangulator, in *Applied Computational Geometry: Towards Geometric Engineering, Lecture Notes in Computer Science*, edited by M. C. Lin, and D. Manocha, pp. 203–222, vol. 1148, Springer-Verlag, Berlin.
- Simo, J. C., and T. J. R. Hughes (2004), *Computational Inelasticity*, Springer, New York.
- Sobolev, S., and A. Babeyko (2005), What drives orogeny in the Andes?, *Geology*, 33, 617–620, doi:10.1130/G21557AR.1.
- Tackley, P. J. (2000), Self-consistent generation of tectonic plates in time-dependent, three-dimensional mantle convection simulations, *Geochem. Geophys. Geosyst.*, 1, 1021, doi:10.1029/2000GC000036.
- Tan, E., L. L. Lavier, H. J. A. Van Avendonk, and A. Heuret (2012), The role of frictional strength on plate coupling at the subduction interface, *Geochem. Geophys. Geosyst.*, 13, Q10006, doi:10.1029/2012GC004214.
- Trangenstein, J. A. (1994), A second-order Godunov algorithm for two-dimensional solid mechanics, *Comput. Mech.*, 13 (5), 343–359, doi:10.1007/BF00512588.
- Trangenstein, J. A., and P. Colella (1991), A higher-order Godunov method for modeling finite deformation in elastic-plastic solids, *Commun. Pure Appl. Math.*, 44(1), 41–100, doi:10.1002/cpa.3160440103.
- Turcotte, D. L., and G. Schubert (2002), *Geodynamics*, 2nd ed., 472 pp., Cambridge University Press, New York.
- van Hunen, J., A. P. van den Berg, and N. J. Vlaar (2001), Latent heat effects of the major mantle phase transitions on low-angle subduction, *Earth Planet. Sci. Lett.*, 190(3-4), 125–135, doi:10.1016/S0012-821X(01)00383-1.
- van Keeken, P. E., S. D. King, H. Schmeling, U. R. Christensen, D. Neumeister, and M.-P. Doin (1997), A comparison of methods for the modeling of thermochemical convection, *J. Geophys. Res.*, 102(B10), 22,477–22,495, doi:10.1029/97JB01353.
- Čížková, H., J. van Hunen, A. P. van den Berg, and N. J. Vlaar (2002), The influence of rheological weakening and yield stress on the interaction of slabs with the 670 km discontinuity, *Earth Planet. Sci. Lett.*, 199(3-4), 447–457, doi:10.1016/S0012-821X(02)00586-1.
- Watts, A., and E. Burrov (2003), Lithospheric strength and its relationship to the elastic and seismogenic layer thickness, *Earth Planet. Sci. Lett.*, 213(1-2), 113–131, doi:10.1016/S0012-821X(03)00289-9.
- Watts, A. B. (2001), *Isostasy and Flexure of the Lithosphere*, Cambridge University Press, Cambridge, U.K.
- Wilkins, M. L. (1964), Calculations of elastic-plastic flow, in *Methods in Computational Physics*, edited by B. Alder, S. Fermback, and M. Rotenberg, pp. 211–264, Academic Press, New York.
- Yamamoto, Y., R. Hino, and M. Shinohara (2011), Mantle wedge structure in the Miyagi prefecture forearc region, central northeastern Japan arc, and its relation to corner-flow pattern and interplate coupling, *J. Geophys. Res.*, 116, B10,310, doi:10.1029/2011JB008470.